Energy 245 (2022) 123198

Contents lists available at ScienceDirect

Energy

journal homepage: www.elsevier.com/locate/energy

# Multi-objective optimization and multi-aspect analysis of an innovative geothermal-based multi-generation energy system for power, cooling, hydrogen, and freshwater production

Kun Li [a, b, 1], Yi-Zhe Ding [c, 1], Chen Ai [d, 1], Hongwei Sun [a, b, *], Yi-Peng Xu [e, 1, **], Navid Nedaei [f]

[a] Shandong Provincial University Laboratory for Protected Horticulture, Weifang University of Science and Technology, Shandong, 262700, China
[b] Weifang Key Laboratory of Blockchain on Agricultural Vegetables, Weifang University of Science and Technology, Shandong, 262700, China
[c] Bussiness School, Sichuan University, Sichuan, 610065, China
[d] School of Sciences, Nanchang University, Jiangxi, 330000, China
[e] School of Mathematical Sciences, Tiangong University, Tianjin, 300387, China
[f] Department of Mechanical Engineering, University of Tabriz, Tabriz, 51666-14766, Iran

ARTICLE INFO

*Article history:*
Received 28 October 2021
Received in revised form
16 December 2021
Accepted 12 January 2022
Available online 17 January 2022

*Keywords:*
Geothermal energy
Innovative heat recovery
Multi-generation
Multi-objective optimization
Sensitivity analysis

ABSTRACT

Considering the feasibility of geothermal wells employed worldwide in the energy sector, this study was motivated to examine a novel multi-generation system devised to enhance the feasibility of flash-binary geothermal systems through innovative heat recovery in five stages. Accordingly, the main system consists of a flash-binary geothermal cycle, an ejector refrigeration cycle, a Kalina cycle integrated with another ejector refrigeration cycle, a humidification dehumidification desalination unit, and a low-temperature electrolyzer. Due to the five stages of innovative heat recovery, this system achieved a cost-effective and efficient design framework, introducing it as a high-quality alternative for stand-alone flash-binary geothermal cycles. To study the feasibility of the proposed system, a sensitivity analysis based on energy, exergy, and exergoeconomic concepts was employed. Moreover, the genetic algorithm in different multi-objective optimization scenarios was implemented to reach stable and high-efficiency products. According to the obtained results, the capability of the system to produce electricity, cooling, freshwater, and hydrogen are calculated to be 782 kW, 881.6 kW, 0.286 kg/s, and 0.181 kg/h, respectively. Also, in the exergy-cost optimization scenario, the system's optimum exergy efficiency and sum unit cost of products were obtained to be 46.44% and 3.98 $/GJ, respectively based on LINMAP decision-making method.



## 1. Introduction

Energy is essential in practically every aspect of our lives, including its production and use, which has a direct impact on the environment [1,2]. Due to the undesirable situation carried out by conventional energy conversion systems producing the sole product or operating with fuels generating high emissions [3], the utilization of polygeneration systems driven by green and renewable energy sources through an efficient framework is an innovative idea to control the current position of environment and energy economy throughout the world [4]. Consequently, the introduction, assessment, and development of such systems are considered essential undertakings for engineers, researchers, and companies active in the field of energy conversion [5].

As a principal renewable energy source, geothermal energy is the heat extracted from the earth in different forms [6]. Owing to the continuous decay of radioactive within the underground plates, the earth can emit thermal energy for billions of years into the future [7]. Respecting the distinct levels of maturity based on thermodynamic conditions of the geothermal fluid extracted,

* Corresponding author. Shandong Provincial University Laboratory for Protected Horticulture, Weifang University of Science and Technology, Shandong 262700, China.
** Corresponding author.
*E-mail addresses:* sunhongwei_doctor@yeah.net (H. Sun), Yi-Peng.Xu@outlook.com (Y.-P. Xu).
[1] These authors contribute equally to this paper.

https://doi.org/10.1016/j.energy.2022.123198
0360-5442/

**Nomenclature**

| | |
|---|---|
| $A$ | Area ($m^2$) |
| $ANS$ | Annual net saving money ($) |
| $AI$ | Annual income ($) |
| $c$ | Unit exergy cost($/GJ) |
| $\dot{C}$ | Cost rate ($/h) |
| $C_p$ | Specific heat at constant pressure ($kJ/kgK$) |
| $CRF$ | Capital recovery factor |
| $D$ | Membrane thickness ($\mu m$) |
| $E_{act}$ | Activation energy ($kJ/kmol$) |
| $\dot{E}x$ | Exergy rate ($kW$) |
| $\dot{E}x_D$ | Exergy destruction rate ($kW$) |
| $F$ | Faraday constant ($C/mol$) |
| $FC$ | Fixed cost ($) |
| $GOR$ | Gain output ratio |
| $h$ | Specific enthalpy ($kJ/kg$) |
| $i$ | Current density ($A/m^2$) |
| $i_r$ | Annual interest rate (%) |
| $IF$ | Inflation factor |
| $\dot{m}$ | Mass flow rate ($kg/s$) |
| $MR$ | Mass ratio |
| $N$ | Annual operating time ($h$) |
| $\dot{n}$ | Molar flow rate |
| $NPV$ | Net present value |
| $OC$ | Operating cost ($) |
| $P$ | Pressure ($kPa$) |
| $PP$ | Payback period ($year$) |
| $\dot{Q}$ | Heat transfer rate ($kW$) |
| $r_p$ | Pressure ratio |
| $R$ | Inflation rate (%) |
| $R_{PEME}$ | Total Ohmic resistance (Ω) |
| $RDF$ | Real discount factor |
| $RIR$ | Real interest rate (%) |
| $s$ | Specific entropy ($kJ/kgK$) |
| $T$ | Temperature ($K$) |
| $U$ | Heat loss coefficient ($W/m^2K$) |
| $u$ | Velocity ($m/s$) |
| $V$ | Voltage ($V$) |
| $\dot{W}$ | Power or work ($kW$) |
| $Z$ | Purchase cost ($) |
| $\dot{Z}$ | Investment cost rate ($/h) |

*Greek symbols*

| | |
|---|---|
| $\varepsilon$ | Effectiveness |
| $\eta$ | Efficiency (%) |
| $\lambda$ | Water content ($\Omega^{-1}$) |
| $\mu$ | Entrainment ratio |
| $\sigma$ | Ionic conductivity |
| $\varphi$ | Maintenance factor |
| $\omega$ | Relative humidity |

*Subscripts*

| | |
|---|---|
| 0 | Reference condition |
| $a$ | Anode |
| $act$ | activation |
| $c$ | Cathode |
| $ch$ | Chemical |
| $d$ | Diffuser |
| $en$ | Energy |
| $ex$ | Exergy |
| $F$ | Fuel |
| $fw$ | Freshwater |
| $in$ | Inlet |
| $is$ | Isentropic |
| $k$ | Control volume k |
| $L$ | Lost |
| $n$ | Nozzle |
| $net$ | Net |
| $m$ | Mixer |
| $out$ | Outlet |
| $ohm$ | Ohmic |
| $P$ | Product |
| $ph$ | Physical |
| $PY$ | present year |
| $total$ | Total |
| $u$ | Useful |

various applications of geothermal technologies can be projected [8]. The electricity production from hydrothermal geothermal reservoirs has widely been working since 1913. In this regard, dry steam and flash-binary cycles are recognized as the prevalent technologies for heat-to-power and cogeneration applications [9]. Because of the baseload feature of the geothermal systems, they can generate energy independent of climate change. Therefore, geothermal energy is a good alternative for energy conversion systems and an attractive option to meet the energy demand of regions near geothermal sources [10]. Accordingly, some recent papers about geothermal polygeneration systems and their applications have been reviewed next.

Yuksel and Ozturk [11] thermodynamically and economically studied a geothermal polygeneration system producing power, hydrogen, cooling, and heating. They used a flash-binary geothermal cycle integrated with an organic Rankine cycle (ORC), a quadruple effect absorption chiller, and a proton exchange membrane electrolyzer (PEME), reaching the overall energy and exergy efficiencies of 47% and 32%, and hydrogen generation cost of 1.1 $/kg. Boyaghchi and Safari [12] developed a quadruple energy production system based on geothermal energy to produce four types of products, namely electrical power, heating load for vaporizing liquefied natural gas, cooling effect, and hydrogen. The energy and exergy efficiencies of their proposed system were obtained by 82.6% and 38.2%, respectively. A comparative study and optimization of using different organic working fluids in an ORC integrated with a flash-binary geothermal cycle were carried out from the thermodynamic and economic viewpoints by Aali et al. [13]. It was found that the R141b was the best working fluid thanks to the thermodynamic and economic analyses with exergy efficiency and electrical unit exergy cost of 52.6% and 4.9 $/GJ, respectively. Considering the geothermal water temperature between 110 °C and 150 °C, Erdeweghe et al. [14] investigated the capability of four configurations of a power and heat cogeneration system consisting of an ORC and a direct heating system. Their newly devised HB4 system was the best among the other configurations combined with a geothermal source. Salehi et al. [15] comparatively assessed and optimized two geothermal-based systems; the first consists of a double-flash binary geothermal cycle and a desalination unit, and the second employed the mentioned subsystems together with a heat transformer. The improved system reached the highest capability with an exergy efficiency of 54.6%

compared to the first system. Calise et al. [16] proposed and apprised a geothermal-based system for power production and thermal drying of wastewater sludge on a small island in Italy. Their study showed a net present value of 502,000 € and a payback period (PP) of 8.3 years.

Integration of a cascade ORC and an absorption chiller with a geothermal resource based on data of Torre Alfina in Italy was studied by Leveni et al. [17]. They implemented a thermodynamic analysis, and the exergy efficiency was obtained to be 27.7%. Ebadollahi et al. [18] devised a polygeneration system utilizing geothermal energy comprising an ORC, an ejector refrigeration cycle (ERC), a liquid natural gas (LNG) power production unit, and a PEME. Based on their results, the energy and exergy efficiencies and sum unit cost of products (SUCP) were computed as 38.3%, 28.9%, and 347.9 $/GJ, respectively. Temiz and Dincer [19] employed solar and geothermal energies in a polygeneration system regarding the climate conditions of Canakkale, Turkey. Their goal was simultaneous production of power, freshwater, and hydrogen, whereby the energy and exergy efficiencies were obtained by16.3% and 14.9%, respectively. Moreover, the calculations demonstrated a SUCP of 0.058 $/kWh for the proposed plant. Kurşun [20] proposed a geothermal-based and solar-assisted polygeneration system utilizing photovoltaic solar collectors. Also, they used an ORC, a PEME, and an absorption chiller as subsystems of the whole system. Wang et al. [21] suggested the integration of an absorption chiller with a flash-binary geothermal cycle for the simultaneous production of power, cooling, and heating. As a result, the exergy efficiency was obtained to be 43.7%. Using solar and geothermal energies, Karapekmez and Dincer [22] suggested a polygeneration system with six outputs consisting of electricity, cooling, heating, hydrogen, hot water, and dry air. Consequently, the energy and exergy efficiencies of the system were 78.4% and 58.4%, respectively. Li et al. [23] thermodynamically and economically investigated and optimized a system embracing a geothermal cycle, an organic flash cycle (OFC), and a proton exchange membrane fuel cell (PEMFC). Their system employed an optimum inlet temperature of 116 $^{\circ}C$, whereby the optimum exergy efficiency and cost rate were equal to 18.7% and 10.5 $/h. Cao et al. [24] devised a geothermal-driven dual-pressure ORC integrated with a PEME for the simultaneous production of electricity and hydrogen, wherein a comparative study of different organic working fluids was carried out. Their study addressed R123 as the best organic working fluid.

Parikhani et al. [25] modified a flash-binary geothermal cycle using an ejector and enhanced its electricity production capacity and economic capability in a novel framework. The modified system correspondingly reached the optimum energy and exergy efficiencies of 7.6% and 41.7%. With a multi-heat recovery technique, Cao et al. [26] developed, studied, and optimized a double flash-binary geothermal cycle coupled with a Kalina cycle, a PEME, and a reverse osmosis unit producing electricity, hydrogen, and freshwater. Their optimization showed the optimum exergy efficiency and hydrogen and freshwater production rates of 51.3%, 5.3 kg/h, and 19.9 kg/s, respectively. Assessment of a system consisting of a geothermal cycle, a Kalina cycle, an absorption chiller, and a PEME was accomplished by Azariyan et al. [27]. They parametrically analyzed the system and found the exergy efficiency and SUCP of 21.4% and 29.3 $/GJ, respectively. Musharavati et al. [28] worked on a system producing power, cooling, heating, and freshwater. This system was configured using a flash-binary geothermal cycle, photovoltaic solar collectors, an OFC, and an absorption chiller. They optimized their system, in which the optimum exergy efficiency and electrical cost rate were equal to 43.6% and 112.1 $/h, respectively. In a study by Leveni and Cozzolino [29], the feasibility of incorporating a modified Goswami cycle with a geothermal cycle was investigated and compared with a combined cycle of an ORC, an absorption chiller, and a geothermal cycle. Consequently, the modified Goswami cycle performed the best thermodynamic and economic performances with the energy efficiency and total investment cost of 35.5% and 11.8 M€. Cao et al. [30] proposed a polygeneration system, in which a double-flash binary geothermal system, an ORC coupled with an ERC, and a PEME were established. Their optimization illustrated an exergy efficiency of 35.8%, leading to a SUCP of 18.8 $/GJ. Ansarinasab et al. [31] performed a life cycle assessment of a geothermal-based multigeneration system using LNG cold energy-integration of Kalina cycle, Stirling engine, desalination unit and magnetic refrigeration system. The proposed system could generate 36 ton/h freshwater, 7774 kW net power, 354 ton/h hot water (at 77 °C), and 45 ton/h cold water (at 5 °C). According to different products, the exergy efficiency was obtained to be 42.95%. Ansarinasab and Hajabdollahi [32] developed a novel multi-generation system based on geothermal energy for the simultaneous heating, power, and freshwater production. According to obtained results, at the optimal point, the exergy efficiency of the whole system and product cost rate were obtained to be 52.65% and 4.35 $/GJ, respectively.

➢Main novelties and contributions

Geothermal energy (GE) is a non-carbon renewable energy source that is based on heat flow from the earth's core; it is a dependable and plentiful energy source with enormous potential. This heat is primarily stored in hot rocks at high depths from the earth's surface, and it is also found in complex structures of hydrothermal reservoirs at high temperatures. Based on the availability of exploitable hydrothermal resources, a large number of technologies and power plant configurations have been studied.

Accordingly, the literature survey comprehensively assessed the capability of geothermal polygeneration systems proposed and investigated in previous studies. However, due to the importance of the topic, especially the conditions of living, it is essential to appraise the capability of geothermal energy and perform more studies on geothermal polygeneration systems through novel configurations. Hence, this paper devises a novel geothermal polygeneration system producing electricity, cooling, freshwater, and hydrogen. In essence, this system comprising a flash-binary geothermal cycle, an ERC using steam, a Kalina cycle integrated with another ERC using Isobutane, a HDH desalination, and a PEME. The principal point distinguishing this paper from the literature survey is implementing innovative heat recovery in five different stages at which the cascade heat recovery has been considered. Furthermore, the energy, exergy, economic (exergoeconomic and NPV) analyses and multi-objective optimization in four cases are conducted to study the feasibility of the proposed system. To this end, sensitivity analysis of the performance indicators based on six crucial parameters, and a genetic algorithm and LINMAP and TOPSIS decision-making methods are utilized for the evaluation.

## 2. System description

As Fig. 1 illustrates, the configuration designed in the current work comprises a flash-binary geothermal cycle as the prime mover integrated with an ERC, a Kalina cycle coupled with an ERC, a HDH unit, and a PEME. Considering the polygeneration system projected in this paper, the geothermal water is extracted at state 1 enters expansion valve 1 (EV1) and delivered to separator 1 (Sep1). Accordingly, the steam and liquid phases of entering water respectively separate into streams 3 and 5, where stream 3 produces power by the steam turbine (ST), and stream 5 makes a heat recovery (first stage). After generating power by the steam turbine, the first ERC is established to yield cooling. Indeed, stream 4 leaving

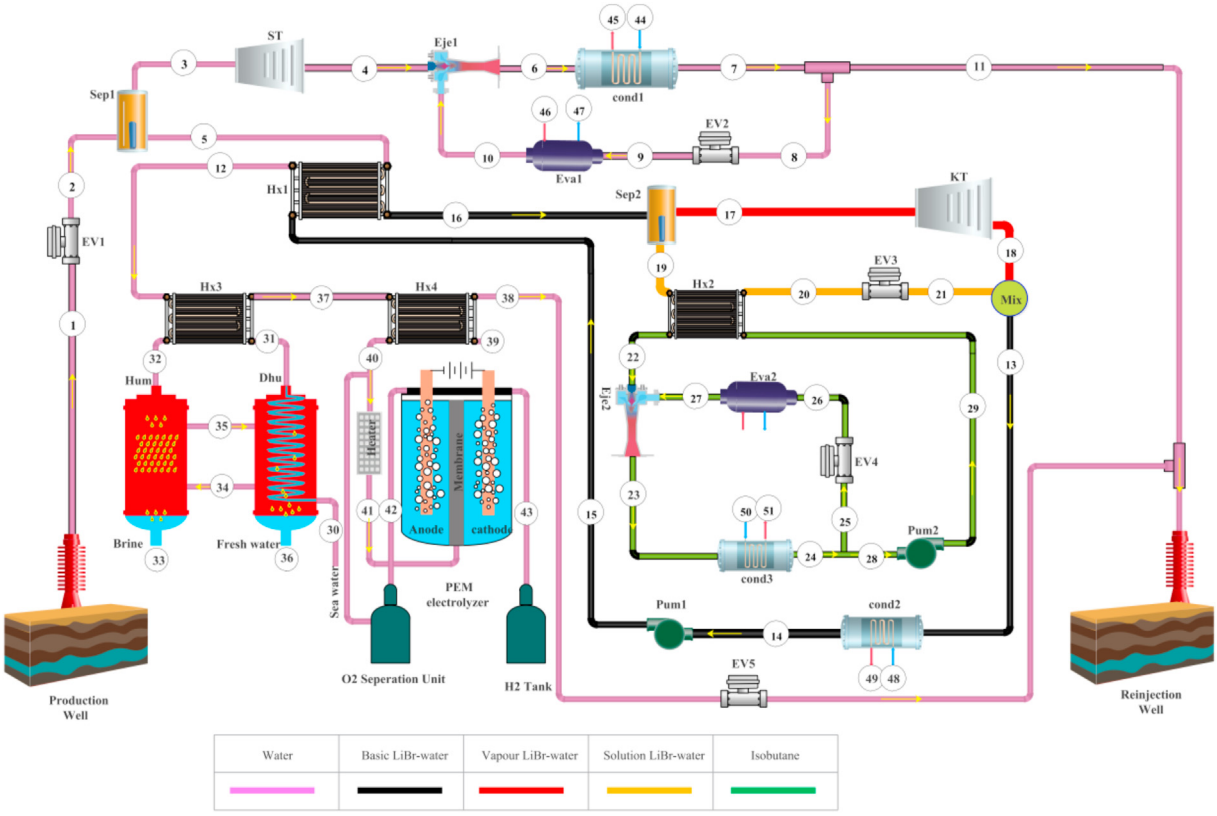


**Fig. 1.** The structure of the geothermal-based multi-generation system devised in the current study.

the steam turbine plays the primary flow role in ejector 1 (Eje1), and stream 10 is its secondary flow. Accordingly, the output flow of the ejector (state 6) is delivered to condenser 1 (cond1) and leaves it at state 7. Besides, stream 7 is divided into streams 8 and 11, where stream 8 passes through expansion valve 2 (EV2) and flows into evaporator 1 (Eva1) at state 9. After producing cooling at state 47, stream 10 is delivered to ejector 1. Also, stream 11 flows into the reinjection well.

On the other hand, stream 5 is used for the second stage of heat recovery via heat exchanger 1 (Hx1). This heat exchanger is recognized as the energy supplier of the Kalina cycle. The base Lithium Bromide-Water ($LiBr-H_2O$) entering heat exchanger 1 at state 15 is heated and leaves this component at state 16. Subsequently, stream 16 goes into separator 2 (Sep2), and the vapor phase (state 17) separated by separator 2, flows into the Kalina turbine to generate power. As the third stage of heat recovery, stream 19 (the solution leaving separator 2) runs heat exchanger 2 (Hx2) of the ERC and exits it at state 20. Stream 20 enters expansion valve 3 (EV3) and flows into the mixer (mix) to mix with stream 18 (the output flow of the Kalina turbine). Besides, the mixture as the base $LiBr-H_2O$ is led to condenser 2 (cond 2); and then pumped by pump 1 (Pum1) from state 14 to state 15 to complete the Kalina cycle.

Isobutane is used as the working fluid of the ERC cycle. The working fluid that is heated by heat exchanger 2 is utilized as the primary flow of ejector 2 (Eje2), and stream 27 is its secondary flow. Accordingly, the output flow of ejector 2 (state 23) is delivered to condenser 3 (cond3), and the saturated liquid leaving this condenser (state 24) is divided into two parts. The first section (state 25) passes through expansion valve 4 (EV4) and goes to evaporator 2 (Eva2) to generate cooling, and the second section (state 28) is pumped by pump 2 (Pum2) to heat exchanger 2 at state 29. As a result, the cooling can be provided through state 53.

The output geothermal water of heat exchanger 1 at state 12 is used to drive heat exchanger 3 (Hx3) at the fourth stage of heat recovery. This heat exchanger is the heater of the HDH unit. The seawater entering the dehumidifier (Dhu) of the HDH is preheated by moist air at state 35 and leaves the dehumidifier at state 31. Also, the moist air losses its moisture as the freshwater at state 36. Besides, stream 34 (dry air leaving the dehumidifier) flows into the humidifier (Hum). Also, stream 32 as the hot seawater enters to the humidifier and wets stream 34 to generate moist air at state 35. Accordingly, the brine is reinjected the sea at state 33.

As the latest stage of heat recovery, stream 37 exiting heat exchanger 3 goes into the heat exchanger 4 (Hx4) to heat input water of the PEME and prepare it for the reactions inside the electrolyzer. Hence, stream 39 is heated by heat exchanger 4 and enters the anode of the PEME at state 41. As a result, after electrolyzing water by the input electricity, the hydrogen can be achieved from the cathode side (state 43), and the anode side yields water and oxygen (state 42). This stream goes into the oxygen separator; the separated water can be recycled.

## 3. Modeling and optimization

The modeling of this paper has been performed via developing a code written in engineering equation solver (EES) software. EES as the heat transfer- and thermodynamic-based software outstandingly assists thermodynamic-based equations due to having a strong database of many working fluids in various operating conditions. Moreover, MATLAB software has been coupled with EES to optimize the calculations and generate Pareto front diagrams. Fig. 2 illustrates the simulation and optimization steps of this work.

Also, the following assumptions and the input data tabulated in

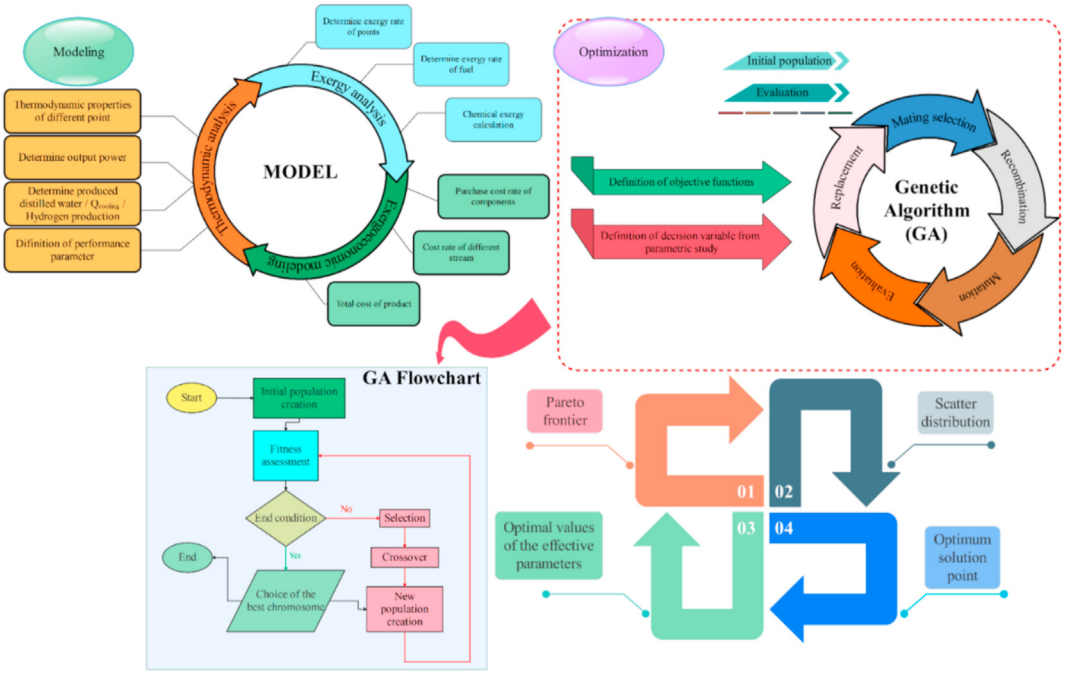


**Fig. 2.** The flowchart of simulation and optimization processes of the current study.

**Table 1**
In data for modeling [36–39].

| Parameter | Value | Unit |
|---|---|---|
| Reference pressure, $P_0$ | 101.3 | kPa |
| Reference temperature, $T_0$ | 298.15 | kPa |
| Mass flow rate of geothermal water, $\dot{m}_{gw}$ | 10 | kg/s |
| Specific enthalpy of geothermal water, h | 1000 | kJ/kg |
| Pressure of well production, $P_1$ | 1200 | kPa |
| Pressure of separator, $P_2$ | 600 | kPa |
| Pressure ratio of steam turbine, $r_p$ | 10 | – |
| Temperature of condenser 1, $T_7$ | 303.15 | K |
| Temperature of evaporator 1, $T_{10}$ | 273.15 | K |
| Temperature of evaporator 2, $T_{27}$ | 280 | K |
| Temperature of condenser 3, $T_{24}$ | 310 | K |
| Pressure of condenser 1, $P_{14}$ | 998.78 | kPa |
| Isentropic efficiency of ST, $\eta_{is,ST}$ | 85 | % |
| Isentropic efficiency of KT, $\eta_{is,KT}$ | 80 | % |
| Isentropic efficiency of Pumps, $\eta_{is,ST}$ | 70 | % |
| Pressure of Pump 1, $P_{15}$ | 3548.23 | kPa |
| Terminal Temperature difference of Hx 1, TTDhx1 | 15 | K |
| Terminal Temperature difference of Hx 2, TTDhx2 | 15 | K |
| Concentration of basic ammonia-water | 85 | % |
| Cooling water temperature of condensers | 298.15 | % |
| Salinity of seawater | 35 | g/kg |
| PEM working Temperature | 353.15 | K |
| Oxygen pressure, $P_{O2}$ | 100 | kPa |
| Hydrogen pressure, $P_{H2}$ | 100 | KPa |
| Faraday constant, F | 96486 | c/mol |
| Water content at the anode-membrane interface, $\lambda_a$ | 14 | $\Omega^{-1}$ |
| Water content at the cathode-membrane interface, $\lambda_c$ | 10 | $\Omega^{-1}$ |
| Membrane thickness, D | 100 | $\mu$m |
| Anode pre-exponential factor, $i_a^{ref}$ | 170000 | A/m$^2$ |
| Cathode pre-exponential factor, $i_c^{ref}$ | 4600 | A/m$^2$ |
| Activation energy in cathode, $E_{act,a}$ | 76 | kJ/mol |
| Activation energy in cathode, $E_{act,c}$ | 18 | kJ/mol |
| Salinity of seawater, S | 35 | g/kg |
| Desalination mass flow rate ratio, MR | 2.333 | – |
| Air relative humidity, ∅ | 90 | % |

Table 1 are utilized in the simulation process [33–35].

- Considering steady-state conations for operation of the system.
- Neglecting the pressure drop inside the heat exchanging devices and piping network.
- Neglecting the heat loss of the components.
- Neglecting the potential and kinetic energies and exergies.
- Considering isentropic efficiency for the turbines and pumps.
- Considering saturated conditions for the inlet of the evaporators and outlet of the condensers.
- Considering one-dimensional ejectors with homogeneous flows.
- Considering adiabatic walls for the ejectors.
- Considering constant pressure for the primary and secondary flows of the ejectors throughout the mixing process.
- Considering the freshwater temperature as the average amount of the two temperatures, i.e., temperature of the moist air and dry air.

### 3.1. Thermodynamic analysis

Generally, the mass and energy conservations of each control volume as the base equations respecting the first law of thermodynamics are presented as follows [40]:

$$\sum \dot{m}_{in,k} - \sum \dot{m}_{out,k} = 0 \tag{1}$$

$$\dot{Q}_k - \dot{W}_k = \sum \dot{m}_{out,k} h_{out,k} - \sum \dot{m}_{in,k} h_{in,k} \tag{2}$$

where $\dot{m}$, $\dot{Q}_k$, and $\dot{W}_k$ are the mass flow rate, the heat transfer rate of the kth control volume, and power of the kth control volume, respectively.

Exergy is defined as the maximum useful work available throughout a process bringing the system and surrounding in an equilibrium. Thus, two exergies are considered in this paper; namely, physical ($\dot{E}x_{ph}$) and chemical ($\dot{E}x_{ch}$) exergy rates. For the stream *i*, it can be written that [40]:

$$\dot{E}x_{ph,i} = \dot{m}_i((h_i - h_{0,i}) - T_0(s_i - s_{0,i})) \quad (3)$$

$$\dot{E}x_{ch,i} = \dot{n}_i\left(\sum y_e \overline{ex}_e^{ch,o} + \overline{R}T_0 \sum y_e \ln(y_e)\right) \quad (4)$$

where ṅ, s, y, and $\overline{ex}^{ch,o}$ present the molar flow rate, specific entropy, molar fraction, and standard chemical exergy, respectively. Also, subscript *"e"* shows the species of the ith stream.

Consequently, the exergy destruction equation can be presented as follows [40]:

$$\dot{E}x_{D,k} = \sum_j \left(1 - \frac{T_0}{T_j}\right)\dot{Q}_{j,k} - \dot{W}_{cw,k} + \sum_i \dot{E}x_{in,k} - \sum_e \dot{E}x_{out,k} \quad (5)$$

Here, the terms $\left(1 - \frac{T_0}{T_j}\right)\dot{Q}_{j,k}$ and $\dot{W}_{cw,k}$ show the exergy rate of the heat loss and power, respectively. Also, $\dot{E}x_{in,k}$ and $\dot{E}x_{out,k}$ are the exergy rate of the input and output streams, respectively.

Also, the exergy destruction equation can be expressed as [40]:

$$\dot{E}x_{D,k} = \dot{E}x_{F,k} - \dot{E}x_{P,k} \quad (6)$$

where $\dot{E}x_{F,k}$ and $\dot{E}x_{P,k}$ are the fuel exergy rate and product exergy rate for the kth control volume.

Besides, the exergy efficiency of the kth control volume is determined by Ref. [40]:

$$\eta_{ex,k} = \frac{\dot{E}_{P,k}}{\dot{E}_{F,k}} \quad (7)$$

Accordingly, the modeling of the ejector, HDH unit, and PEME are presented in supplementary materials. Also, Table 1s provides all mass, energy, and exergy conservations equations for the components used in proposed plant.

Based on thermodynamic laws, the performance indicators of the system proposed in this paper are presented next. Therefore, the cooling, freshwater, and hydrogen production rates are determined through the following equations [13]:

$$\dot{Q}_{cooling} = \dot{m}_{46}(h_{46} - h_{47}) + \dot{m}_{52}(h_{52} - h_{53}) \quad (8)$$

$$\dot{m}_{fw} = \dot{m}_{36} \quad (9)$$

$$\dot{m}_{H2} = 3600 \times \dot{m}_{43} \quad (10)$$

Also, the energy and exergy efficiencies can be defined by Ref. [13]:

$$\eta_{th} = \frac{\dot{W}_{net} + \dot{Q}_{cooling} + \dot{m}_{36}h_{fg} + \dot{m}_{43}LHV_{H2}}{\dot{m}_1 h_1 - \dot{m}_{55}h_{55}} \quad (11)$$

$$\eta_{ex} = \frac{\dot{W}_{net} + (\dot{E}x_{47} - \dot{E}x_{46}) + (\dot{E}x_{53} - \dot{E}x_{52}) + \dot{m}_{36}ex_{H2O}^{ch,o} + \dot{m}_{43}ex_{H2}^{ch,o}}{\dot{E}x_1 - \dot{E}x_{55}} \quad (12)$$

### 3.2. Economic analysis

The economic assessment carried out in this paper consisting of exergoeconomic analysis and NPV (net present value) method. Regarding the use of exergy concept in economics, the following cost balance equation can be utilized for the kth control volume [41]:

$$\dot{C}_{q,k} + \sum \dot{C}_{in,k} + \dot{Z}_k = \dot{C}_{w,k} + \sum \dot{C}_{out,k} \quad (13)$$

where [29].

$$\dot{C}_{q,k} = c_q\left(1 - \frac{T_0}{T_{j,k}}\right)\dot{Q}_{j,k} \quad (14)$$

$$\dot{C}_{w,k} = c_w\dot{W}_{cw,k} \quad (15)$$

$$\dot{C}_{in,k} = c_{in}\dot{E}_{in,k} \quad (16)$$

$$\dot{C}_{out,k} = c_{out}\dot{E}_{out,k} \quad (17)$$

where $\dot{C}$ is the cost rate and c is the unit exergy cost.

Moreover, $\dot{Z}_k$ represents the investment cost rate of the kth control volume; this variable has the following relation with the purchase cost ($Z_k$), capital recovery factor (*CRF*), maintenance factor ($\varphi$), and annual operating time ($N$) [41].

$$\dot{Z}_k = \frac{Z_k \times CRF \times \varphi}{N} \quad (18)$$

Also,

$$CRF = \frac{i_r(1 + i_r)^n}{(1 + i_r)^n - 1} \quad (19)$$

where $i_r$ and $n$ are the interest rate and lifetime of the system, respectively.

The investment cost rate of the kth component should be updated through [41]:

$$\dot{Z}_{k,PY} = \dot{Z}_{k,reference} \times \frac{CI_{PY}}{CI_{reference}} \quad (20)$$

where $CI_{PY}$ and $CI_{reference}$ depict the chemical index of the plant at the present and reference years, respectively. Bedsides, Table 2 lists the general cost balance equation and auxiliary for the components used in the proposed system. Also, Table 3 contains the purchased cost functions of the components. As Table 3 depicts, the heat transfer area of the heat transfer-based equipment can be found by Ref. [41]:

$$A_k = \frac{\dot{Q}_k}{U_k \Delta T_{LMTD,k}} \quad (21)$$

where $U_k$ is the overall heat loss coefficient of the kth heat exchanger and $\Delta T_{LMTD,k}$ is its logarithmic mean temperature difference.

Hence [41],

$$\Delta T_{LMTD,k} = \frac{\Delta T_{HotT,k} - \Delta T_{ColdT,k}}{\ln\left(\frac{\Delta T_{HotT,k}}{\Delta T_{ColdT,k}}\right)} \quad (22)$$

where $\Delta T_{HotT,k}$ and $\Delta T_{ColdT,k}$ are respectively hot end and cold end terminal temperature differences of the kth heat exchanger.

The estimation of the overall heat transfer coefficient is an important and frequently the most uncertain aspect of any heat exchanger investigation. Heat transfer coefficient ($U$) is strongly

**Table 2**
Cost rate balances and auxiliary equations for the components of the proposed multi-generation system [41].

| Component | Cost rate balance | Auxiliary equations |
|---|---|---|
| Expansion valve 1 | $\dot{C}_2 = \dot{C}_1 + \dot{Z}_{E.V.1}$ | - |
| Separator 1 | $\dot{C}_2 + \dot{Z}_{Sep} = \dot{C}_3 + \dot{C}_5$ | $c_3 = c_5$ |
| Steam turbine | $\dot{C}_3 + \dot{C}_{W,KT} = \dot{C}_4 + \dot{Z}_{KT}$ | $c_3 = c_4$ |
| Ejector 1 | $\dot{C}_4 + \dot{C}_{10} + \dot{Z}_{eje1} = \dot{C}_6$ | – |
| Condenser 1 | $\dot{C}_6 + \dot{C}_{44} + \dot{Z}_{con1} = \dot{C}_7 + \dot{C}_{45}$ | $c_6 = c_7, c_{44} = 0$ |
| Expansion valve 2 | $\dot{C}_9 = \dot{C}_8 + \dot{Z}_{E.V.2}$ | - |
| Evaporator 1 | $\dot{C}_9 + \dot{C}_{46} + \dot{Z}_{Eva1} = \dot{C}_{10} + \dot{C}_{47}$ | $c_9 = c_{10}$ |
| Heat exchanger 1 | $\dot{C}_5 + \dot{C}_{15} + \dot{Z}_{Hx1} = \dot{C}_{12} + \dot{C}_{16}$ | $c_5 = c_{12}$ |
| Condenser 2 | $\dot{C}_{13} + \dot{C}_{48} + \dot{Z}_{con2} = \dot{C}_{14} + \dot{C}_{49}$ | $c_{13} = c_{14}, c_{48} = 0$ |
| Pump 1 | $\dot{C}_{14} + \dot{C}_{W,Pu1} + \dot{Z}_{Pu1} = \dot{C}_{15}$ | $c_{W,Pu1} = c_{W,ST}$ |
| Separator 2 | $\dot{C}_{16} + \dot{Z}_{Sep1} = \dot{C}_{17} + \dot{C}_{19}$ | $c_{17} = c_{19}$ |
| Kalina turbine | $\dot{C}_{17} + \dot{Z}_{ST} = \dot{C}_{18} + \dot{C}_{W,ST}$ | $c_{17} = c_{18}$ |
| Heat exchanger 2 | $\dot{C}_{19} + \dot{C}_{29} + \dot{Z}_{Hx2} = \dot{C}_{20} + \dot{C}_{22}$ | $c_{19} = c_{20}$ |
| Expansion valve 3 | $\dot{C}_{21} = \dot{C}_{20} + \dot{Z}_{E.V.3}$ | - |
| Mixer | $\dot{C}_{18} + \dot{C}_{21} + \dot{Z}_{Mix} = \dot{C}_{13}$ | - |
| Pump 2 | $\dot{C}_{28} + \dot{C}_{W,Pu2} + \dot{Z}_{Pu2} = \dot{C}_{29}$ | $c_{W,Pu2} = c_{W,ST}$ |
| Ejector 2 | $\dot{C}_{22} + \dot{C}_{27} + \dot{Z}_{eje2} = \dot{C}_{23}$ | – |
| Condenser 3 | $\dot{C}_{23} + \dot{C}_{50} + \dot{Z}_{con3} = \dot{C}_{24} + \dot{C}_{51}$ | $c_{23} = c_{24}, c_{50} = 0$ |
| Expansion valve 4 | $\dot{C}_{25} + \dot{Z}_{E.V.4} = \dot{C}_{26}$ | - |
| Evaporator 2 | $\dot{C}_{26} + \dot{C}_{52} + \dot{Z}_{Eva2} = \dot{C}_{27} + \dot{C}_{53}$ | $c_{26} = c_{27}$ |
| Heat exchanger 3 | $\dot{C}_{12} + \dot{C}_{31} + \dot{Z}_{Hx3} = \dot{C}_{32} + \dot{C}_{37}$ | $c_{12} = c_{37}$ |
| Humidifier | $\dot{C}_{32} + \dot{C}_{34} + \dot{Z}_{Hum} = \dot{C}_{33} + \dot{C}_{35}$ | $c_{32} = c_{33}$ |
| Dehumidifier | $\dot{C}_{30} + \dot{C}_{35} + \dot{Z}_{Dhu} = \dot{C}_{31} + \dot{C}_{34} + \dot{C}_{36}$ | $c_{30} = 0$<br>$c_{34} = c_{35}$<br>$\frac{\dot{C}_{34} - \dot{C}_{30}}{\dot{E}x_{34} - \dot{E}x_{30}} = \frac{\dot{C}_{31} - \dot{C}_{30}}{\dot{E}x_{31} - \dot{E}x_{30}}$ |
| Heat exchanger 4 | $\dot{C}_{37} + \dot{C}_{39} + \dot{Z}_{Hx4} = \dot{C}_{38} + \dot{C}_{40}$ | $c_{37} = c_{38}$ |
| Heater | $\dot{C}_{40} + \dot{C}_{W,Heater} + \dot{Z}_{Heater} = \dot{C}_{41}$ | $c_{W,Heater} = c_{W,ST}$ |
| PEM Electrolyzer | $\dot{C}_{41} + \dot{Z}_{PEM} + \dot{C}_{W,PEM} = \dot{C}_{42} + \dot{C}_{43}$ | $c_{W,PEM} = c_{W,ST}$<br>$c_{42} = c_{43}$ |
| Expansion valve 5 | $\dot{C}_{38} + \dot{Z}_{E.V.5} = \dot{C}_{54}$ | - |

dependent on the heat transferring fluids and their phase. The current work properly calculates the value of $U$ using heat transfer principles. This is in contrast to the bulk of comparable research in the study area, which used a constant $U$-value. As a result of the excellent efficiency and flexibility of counterflow shell-and-tube exchangers, all heat exchangers are counterflow shell-and-tube. A schematic view of a shell-and-tube heat exchanger is drawn in Fig. 3.

The following equation can be used to determine the heat exchanger's $U$-value [43].

$$\frac{1}{U} = \frac{1}{h_{out}} + \frac{1}{h_{in}}\frac{d_o}{d_i} + \frac{d_o}{2k}\ln\left(\frac{d_o}{d_i}\right) \tag{23}$$

where $d_i$, $d_o$, $k$, and $h$ are the inside diameter of the tube, outside diameter of the tube, conductive heat transfer coefficient of the heat exchanger, and convective heat transfer coefficient of the fluids, respectively. The convective heat transfer coefficient can be computed using the Nusselt number definition [42]:

$$h = \frac{k_{fluid} \times Nu}{D_e} \;\&\; D_e = \frac{4A_c}{P} \tag{24}$$

where $k_{fluid}$ and $D_e$ are the conductive heat transfer coefficient and hydraulic mean diameter, respectively. Also, $A_c$ and $P$ present the cross-sectional area for flow and its wetted perimeter, correspondingly.

Two scenarios may be considered in this context when calculating the Nusselt number:

❖Single-phase fluid

For the estimating the heat transfer properties of tube and shell sides in a single-phase fluid, the following equations are used [44].

$$\begin{cases} Nu = 0.023Re^{0.8}\mathrm{Pr}^{1/3}\ , \ for\ tube-side \\ Nu = 0.36Re^{0.55}\mathrm{Pr}^{1/3}\ , \ for\ shell-side \end{cases} \tag{25}$$

All of these thermo-physical characteristics are evaluated at the mean flow temperature of the cold- or hot-side [44]:

$$\begin{cases} T_{m,h} = \dfrac{T_{in,h} + T_{out,h}}{2}\ , \ for\ hot-side \\ T_{m,h} = \dfrac{T_{in,c} + T_{out,c}}{2}\ , \ for\ cold-\ side \end{cases} \tag{26}$$

❖ Two-phase fluid

This situation happens during the condensation or evaporation processes, during which the fluid's thermophysical characteristics undergo drastic changes. The following equations are applied for calculating the Nusselt number for the condensation and evaporation processes [44].

Condensation:

**Table 3**
Purchased equipment cost for the components of the proposed multi-generation system.

| Components | Equation | Ref. Year | Cost index | Ref. |
|---|---|---|---|---|
| Steam turbine | $Z_{ST} = 4405(\dot{W}_{ST})^{0.7}$ | 2003 | 402.3 | [45] |
| Kalina turbine | $Z_{KT} = 4405(\dot{W}_{KT})^{0.7}$ | 2003 | 402.3 | [45] |
| Condenser | $Z_{Cond} = 130\left(\frac{A_{cond}}{0.093}\right)^{0.78}$ | 2005 | 468.2 | [46] |
| Evaporator | $Z_{Eva} = 130\left(\frac{A_{Eva}}{0.093}\right)^{0.78}$ | 2005 | 468.2 | [46] |
| Ejector 1 | $Z_{Eje1} = 1.5 \times 0.45 \times 20 \times \left(\frac{T_4}{P_4}\right)^{0.05} \times P_6^{-0.75}$ | 2010 | 550.8 | [47] |
| Ejector 2 | $Z_{Eje2} = 1.5 \times 0.45 \times 20 \times \left(\frac{T_{22}}{P_{22}}\right)^{0.05} \times P_{23}^{-0.75}$ | 2010 | 550.8 | [47] |
| Pump 1 | $Z_{Pu1} = 3540(\dot{W}_{pu1})^{0.71}$ | 2010 | 550.8 | [45] |
| Pump 2 | $Z_{Pu2} = 3540(\dot{W}_{pu2})^{0.71}$ | 2010 | 550.8 | [45] |
| Heat exchanger | $Z_{Hx} = 130\left(\frac{A_{Hx}}{0.093}\right)^{0.78}$ | 2005 | 468.2 | [45] |
| Mixer | $Z_{Mixer} = 0$ | – | – | [45] |
| Separator | $Z_{Separator} = 0$ | – | – | [45] |
| Expansion valve | $Z_{E.V.} = 114.5 \times \dot{m}_{EV}$ | 2010 | 550 | [47] |
| PEM electrolyzer | $Z_{PEM} = 1000 \times (\dot{W}_{PEM})$ | 2010 | 550.8 | [48] |
| Heater | $Z_{Heater} = 75000 \times (\dot{W}_{heater})^{0.9}$ | 2010 | 550.8 | [48] |
| Humidifier | $Z_{Hum} = 746.759 \times \dot{m}_{30}^{0.79} \times R_1^{0.57} \times A_1^{-0.9924} \times (0.022 \times T_{wb,35} + 0.39)^{2.447}$<br>$R_1 = T_{32} - T_{33}$<br>$A_1 = T_{32} - T_{wb,35}$ | 2010 | 550.8 | [49] |
| Dehumidifier | $Z_{Dhu} = 2143 \times A_{Dhu}^{0.514}$<br>$A_{Dhu} = \dot{m}_{30} \times \frac{h_{31} - h_{30}}{U_{Dhu} \times \Delta T_{lmtd,Dhu}}$<br>$U_{dhu} = 1.4$<br>$\Delta T_{lmtd,Dhu} = \frac{(T_{35} - T_{31}) - (T_{34} - T_{30})}{Ln\left(\frac{T_{35} - T_{31}}{T_{34} - T_{30}}\right)}$ | 2010 | 550.8 | [49] |

Accordingly, the NPV can be calculated by Ref. [41].

$$Nu = 0.023 Re_L^{0.8} \mathrm{Pr}_l^{0.4} \left[ (1 - x_m)^{0.8} + 3.8 \left( \frac{x_m^{0.76} (1 - x_m)^{0.04}}{P^{*0.38}} \right) \right] \tag{27}$$

Evaporation:

Reynolds number of liquid phase, Prandtl number of liquid phase, Reynolds number of saturated liquid, vapor quality, and local heat flux are presented by $Re_l$, $\mathrm{Pr}_l$, $Re_L$, $x_m$, and $\dot{q}$, respectively. In addition, the value $P^*$ stands for reduced pressure ($P^* = \frac{P}{P_{critical}}$).

Note: More information about the heat transfer coefficient determination can be found in Ref. [43].

Also, the fuel and product unit exergy costs are correspondingly formulated by Ref. [41]:

$$c_{F,k} = \frac{\dot{C}_{F,k}}{\dot{E}_{F,k}} \tag{29}$$

$$c_{P,k} = \frac{\dot{C}_{P,k}}{\dot{E}_{P,k}} \tag{30}$$

Consequently, respecting the exergy concept, the exergy destruction cost rate of the kth control volume is [41]:

$$\dot{C}_{D,k} = c_{F,k} \dot{E}_{D,k} \tag{31}$$

As the exergoeconomic performance indicator, sum unit cost of products (SUCP) is determined by Ref. [41]:

$$Nu = \left( \left[ 0.023 F_W Re_l^{0.8} \mathrm{Pr}_l^{0.4} \left( 1 + \frac{1.925}{X_{tt}^{0.83}} \right) \right]^{2.5} + \left[ 55 \dot{q}^{0.67} P^{*0.12} M_{WF}^{-0.5} [(\log P^*)]^{-0.55} \frac{d_i}{k_l} \right]^{2.5} \right)^{1/2.5} \tag{28}$$

$$SUCP = \frac{\dot{C}_{\dot{W}_{net}} + \dot{C}_{36} + \dot{C}_{43} + \dot{C}_{47} + \dot{C}_{53}}{\dot{W}_{net} + \dot{m}_{36} ex_{H2O}^{ch,o} + \dot{m}_{43} ex_{H2}^{ch,o} + \dot{E}x_{47} + \dot{E}x_{53}} \tag{32}$$

$$NPV = -FC + \sum_{i=1}^{n} (ANS \times IF_i \times RDF_i) \tag{33}$$

where *FC* and *ANS* as the principal variables show the fixed cost and annual net saving money, respectively. Also, $IF_i$ and $RDF_i$ present the inflation factor and real discount factor of the ith year during

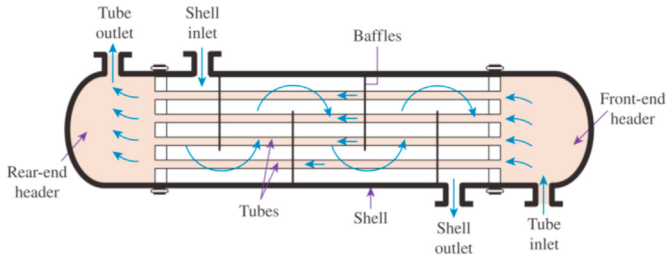


**Fig. 3.** A schematic view of a shell-and-tube heat exchanger [42].

system's lifetime [41].

$$IF_i = \left(1 + \frac{R}{100}\right)^{-i} \tag{34}$$

$$RDF_i = \left(1 + \frac{RIR}{100}\right)^{-i} \tag{35}$$

where $R$ is the inflation rate and $RIR$ is the real interest rate.

Accordingly [41],

$$FC = Z_{invs} + Z_{inst} \tag{36}$$

where $Z_{invs}$ and $Z_{inst}$ depict the total investment cost of the system and total installation and piping cost, correspondingly [41].

$$Z_{invs} = \sum Z_k \tag{37}$$

$$Z_{inst} = 0.1 \times Z_{invs} \tag{38}$$

Afterwards, the annual net saving money as the difference between the annual income ($AI$) and operating cost ($OC$) is formulated as [41]:

$$ANS = AI - OC \tag{39}$$

$$OC = 0.06 \times FC \tag{40}$$

In this way, the payback period of the system is equal to the following relation between the fixed cost and annual net saving money [41]:

$$PP = \frac{FC}{ANS} \tag{41}$$

### 3.3. Multi-objective optimization

The optimization procedure can prepare a well-defined setting respecting the operating framework of the system. In this way, several optimization algorithms are available, wherein a genetic algorithm is a well-developed tool used in many energy conversion-based studies. In essence, this method follows a smart-search phenomenon via a growing strategy inspiring natural selection [50]. The flowchart of this method is shown in Fig. 2. Subsequently, decision variables defined for limiting the optimization are given in Table 4. Hence, the mass flow rate of the inlet geothermal water, its pressure, separator 1 inlet pressure, the pressure ratio of the steam turbine, evaporator 1 inlet temperature, and terminal temperature difference of heat exchanger 1 are the decision variables of the optimization. Also, four ceases of optimization, including the exergy/cost, exergy/cooling, exergy/freshwater, and exergy/hydrogen are considered. To this end, the setting determined below are applied to the MATLAB software:

Number of iteration = 220

Population size = 80

Probability of crossover = 0.85

Probability of mutation = 0.01

Accordingly, the Pareto frontier achieved from the optimization should be analyzed to find the optimal solution. Therefore, a decision-making approach is required to obtain this point. This study uses the LINMAP and TOPSIS decision-making methods. Euclidean distances ($ED$) can be evaluated using the normalized optimal solutions and normalized ideal solutions as follows [51]:

$$ED_i^+ = \sqrt{\sum_{i=1}^{n}\left(ObjF_i^N - ObjF_{i,ideal}^N\right)^2} \tag{42}$$

The normalized objective functions (OFs) can be presented by Ref. [51]:

$$ObjF_i^N = \frac{ObjF_i}{\sqrt{\sum_i (ObjF_i)^2}} \tag{43}$$

The lowest $ED_i^+$ is selected as the final optimum solution using the LINMAP method. In the TOPSIS method, non-ideal points are calculated by Ref. [51]:

$$ED_i^- = \sqrt{\sum_{i=1}^{n}\left(ObjF_i^N - ObjF_{i,non-ideal}^N\right)^2} \tag{44}$$

The relative closeness (RC) is presented by Ref. [51]:

$$RC_i = \frac{ED_i^-}{ED_i^- + ED_i^+} \tag{45}$$

The highest $RC$ is selected as the final optimum solution, with the TOPSIS method.

**Table 4**
The range of decision variables employed to optimize the system.

| Decision variables | Range | Base case value |
|---|---|---|
| $\dot{m}_g$[kg/s] | 5 – 15 | 10 |
| $r_P$[ – ] | 8 – 12 | 10 |
| $P_1$[kPa] | 1000 – 1500 | 1200 |
| $P_2$[kPa] | 450 – 650 | 600 |
| $TTD_{hx1}$[K] | 10 – 20 | 15 |
| $T_{eva1}$[K] | 273.2 – 278.2 | 273.15 |

**Table 5**
Validation of the Kalina cycle; comparison of the results of this study with Ref. [37].

| Item | Ref. [37] | Present study |
|---|---|---|
| Turbine power output (kW) | 199.440 | 199.431 |
| Thermal efficiency (%) | 8.310 | 8.30 |
| Exergy efficiency (%) | 31.26 | 31.27 |
| Basic solution mass flow rate (kg/s) | 2.083 | 2.085 |
| Turbine inlet temperature ($K$) | 393.15 | 393.21 |
| Turbine inlet pressure (kPa) | 3352 | 3352 |

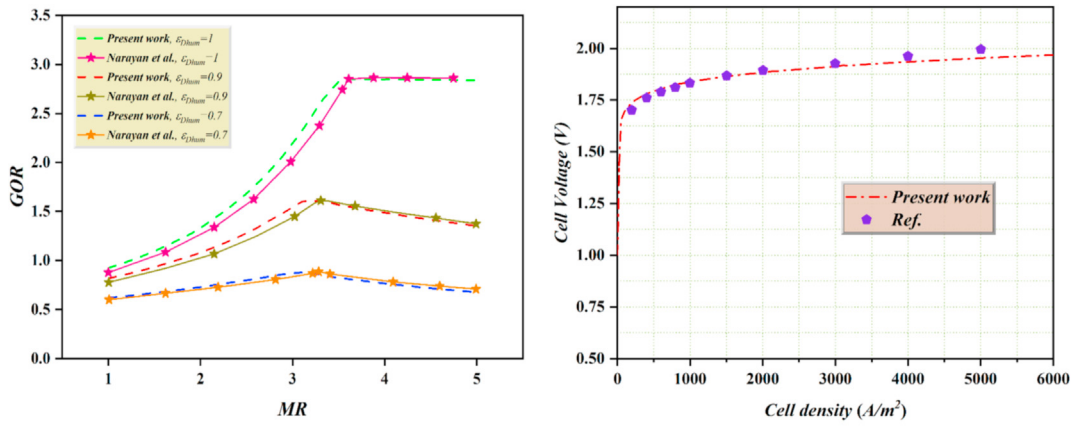


**Fig. 4.** Validation of the (a) HDH unit with Ref. [36] and (b) PEME with Ref. [38].

## 4. Validation

Evaluating the accuracy of the results provided in the current work is accomplished through model validation of the Kalina cycle, HDH unit, and PEME unit. The simulation results of these subsystems are compared with those reported in previous studies, and Table 5 and Fig. 4 report the comparative results.

Table 5 is provided to compare the results of the Kalina cycle modeling; its main performance indicators, including the output power of the Kalina turbine, energy and exergy efficiencies, base solution mass flow rate, and inlet temperature and pressure of the Kalina turbine, are validated in comparison with Du et al. [37] work with a relative error close to zero.

Also, Narayan et al. [36] and Yilmaz et al. [38] works are selected to validate the results of the HDH and PEME modeling, correspondingly (see Fig. 4). In Fig. 4a, the variation in GOR with increasing the mass ratio (between 1 and 5) is plotted for different effectiveness of the dehumidifier. Also, Fig. 4b exhibits the change in cell voltage of the PEME versus different current densities ranging between 0 $A/m^2$ to 6000 $A/m^2$. Fig. 4 measures the relative error below 2%; therefore, the modeling performed in this study possesses high accuracy, and the results are completely justifiable.

## 5. Results and discussion

Considering the analyses performed in this paper, the results are presented in three sections. These sections, which are discussed next, include overall results, results of the sensitivity analysis, and optimization results.

### 5.1. Overall results

To represent the results of the energy and exergy analyses for each state of the proposed multi-generation system suggested in Fig. 1, Table 6 reports the thermodynamic (mass flow rate, temperature, pressure, specific enthalpy, specific entropy, and exergy rate) and exergoeconomic (cost per unit of exergy and cost rate) properties for each state.

Accordingly, Table 7 lists the values of exergy destruction rate and exergy efficiency as the exergetic performance indicators, and unit exergy cost of the fuel and product, exergy destruction cost rate, and investment cost rate as the economic performance indicators for the components of the polygeneration system. To assist this table and demonstrate the contribution of each component in the performance of the whole system, Figs. 5 and 6 are plotted. Generally, based on Table 7 and Fig. 5, ejector 1 is the key irreversibility source of the proposed system with a value of 433.1 *kW*. Also, heat exchanger 1 is the second-worst irreversibility source that its exergy destruction rate is obtained to be 146.8 *kW*. Subsequently, the contribution of the steam turbine and Kalina turbine in the total investment cost rate of the system is higher than other components, where their investment cost rates are 137380 $/year$ and 94506 $/year$, respectively (see Table 7). Also, according to Fig. 6, where the distribution of the purchase cost rate of the components established in the polygeneration system is displayed, the contribution of these turbines in the total investment cost rate of the whole system is found to be 32.91% and 22.64%, respectively. Eventually, the highest exergy destruction cost rate belongs to the dehumidifier and ejector 1 with a value of 74920 $/h$ and 12102 $/h$, respectively.

Fig. 7 shows the Sankey diagram related to the exergy flow of the system. Based on this diagram, a 2632 *kW* exergy rate enters the system, where the electrical exergy rate, cooling exergy rate, freshwater exergy rate, and hydrogen exergy rate obtained are 782 *kW*, 882 *kW*, 2 *kW*, and 6 *kW*, respectively. Also, the total exergy destruction rate of the system is equal to 1178 *kW*.

As the latest overall result, Table 8 lists the overall performance indicators at which the capability of the system to produce electricity, cooling, freshwater, and hydrogen are found to be 782 *kW*, 881.6 *kW*, 0.286 $kg/s$, and 0.181 $kg/h$, correspondingly. Also, this configuration leads to energy and exergy efficiencies of 31.74% and 40.36%, SUCP of 4.76 $/GJ$, and PP of 1.86 *years*.

### 5.2. Results of the sensitivity analysis

Six parameters comprising mass flow rate of the inlet geothermal water, its pressure, separator 1 inlet pressure, the pressure ratio of the steam turbine, evaporator 1 inlet temperature, and terminal temperature difference of heat exchanger 1 are selected for the sensitivity analysis. In addition to this, the sensitivity of the NPV based on the system's lifetime and the variation in the payback period of the system versus the selling price of

**Table 6**
The thermodynamic and exergoeconomic for each state of the multi-generation system.

| Steam | ṁ[kg /s] | T[k] | P[kpa] | h [kJ /kg] | s [kJ /kg.K] | Ėx [kW] | Ċ[$ /year] | c [$ /GJ] |
|---|---|---|---|---|---|---|---|---|
| 1 | 10.00 | 461.15 | 1200.00 | 999.23 | 2.65 | 2631.79 | 90859.74 | 1.37 |
| 2 | 10.00 | 432.01 | 600.00 | 999.23 | 2.69 | 2511.26 | 91303.84 | 1.44 |
| 3 | 1.58 | 432.01 | 600.00 | 2756.69 | 6.76 | 1253.12 | 45560.82 | 1.44 |
| 4 | 1.58 | 359.10 | 60.00 | 2433.21 | 6.92 | 669.04 | 24324.67 | 1.44 |
| 5 | 8.43 | 432.01 | 600.00 | 670.71 | 1.93 | 1258.13 | 45743.02 | 1.44 |
| 6 | 1.95 | 303.15 | 4.25 | 2445.98 | 8.09 | 171.63 | 16898.00 | 3.91 |
| 7 | 1.95 | 303.15 | 4.25 | 125.67 | 0.44 | 97.24 | 9574.57 | 3.91 |
| 8 | 0.37 | 303.15 | 4.25 | 125.67 | 0.44 | 18.45 | 1816.23 | 3.91 |
| 9 | 0.37 | 273.15 | 0.61 | 125.67 | 0.46 | 15.86 | 1832.60 | 4.59 |
| 10 | 0.37 | 273.15 | 0.61 | 2500.52 | 9.15 | − 64.28 | − 7428.06 | 4.59 |
| 11 | 1.58 | 303.15 | 4.25 | 125.67 | 0.44 | 78.80 | 7758.34 | 3.91 |
| 12 | 8.43 | 355.02 | 600.00 | 343.22 | 1.10 | 595.05 | 21634.74 | 1.44 |
| 13 | 1.96 | 364.10 | 9.99 | 1280.77 | 4.33 | 2058.25 | 188178.21 | 3.63 |
| 14 | 1.96 | 302.91 | 9.99 | 31.90 | 0.43 | 1922.14 | 175734.24 | 3.63 |
| 15 | 1.96 | 303.77 | 35.48 | 37.35 | 0.44 | 1929.68 | 187286.51 | 3.85 |
| 16 | 1.96 | 417.01 | 35.48 | 1446.11 | 4.28 | 2445.96 | 220002.96 | 3.57 |
| 17 | 1.69 | 417.01 | 35.48 | 1606.81 | 4.68 | 2255.90 | 206001.33 | 3.62 |
| 18 | 1.69 | 363.37 | 9.99 | 1430.16 | 4.76 | 1914.06 | 174785.23 | 3.62 |
| 19 | 0.27 | 417.01 | 35.48 | 435.22 | 1.79 | 153.33 | 14001.63 | 3.62 |
| 20 | 0.27 | 398.25 | 35.48 | 341.03 | 1.55 | 146.54 | 13381.06 | 3.62 |
| 21 | 0.27 | 367.17 | 9.99 | 341.03 | 1.58 | 144.19 | 13392.99 | 3.69 |
| 22 | 0.07 | 402.01 | 3300.10 | 681.05 | 2.35 | 3294.94 | 3148447.10 | 37.92 |
| 23 | 0.09 | 334.70 | 488.28 | 651.97 | 2.47 | 4381.20 | 4190916.08 | 37.96 |
| 24 | 0.09 | 310.00 | 488.28 | 289.01 | 1.30 | 4379.83 | 4189609.75 | 37.96 |
| 25 | 0.02 | 310.00 | 488.28 | 289.01 | 1.30 | 1090.19 | 1042839.62 | 37.96 |
| 26 | 0.02 | 280.00 | 198.47 | 289.01 | 1.32 | 1090.09 | 1042840.59 | 37.96 |
| 27 | 0.02 | 280.00 | 198.47 | 564.22 | 2.30 | 1089.70 | 1042468.95 | 37.96 |
| 28 | 0.07 | 310.00 | 488.28 | 289.01 | 1.30 | 3289.64 | 3146770.13 | 37.96 |
| 29 | 0.07 | 312.31 | 3300.10 | 295.99 | 1.31 | 3289.99 | 3147653.89 | 37.97 |
| 30 | 5.72 | 298.15 | 101.30 | 99.77 | 0.35 | 0.00 | 0.00 | 0.00 |
| 31 | 5.72 | 330.82 | 101.30 | 230.65 | 0.77 | 38.10 | 57166.22 | 59.55 |
| 32 | 5.72 | 352.60 | 101.30 | 318.30 | 1.02 | 101.79 | 68401.06 | 26.67 |
| 33 | 5.43 | 319.83 | 101.30 | 186.05 | 0.63 | 16.13 | 10841.65 | 26.67 |
| 34 | 2.45 | 314.00 | 101.30 | 159.20 | 6.15 | 4.99 | 7488.80 | 59.55 |
| 35 | 2.74 | 336.56 | 101.30 | 489.45 | 7.17 | 76.99 | 115534.45 | 59.55 |
| 36 | 0.29. | 324.12 | 101.30 | 213.40. | 0.72. | 1.97 | 55487.48 | 1116.31 |
| 37 | 8.43 | 340.82 | 600.00 | 283.72 | 0.93 | 523.40 | 19029.75 | 1.44 |
| 38 | 8.43 | 340.82 | 600.00 | 283.71 | 0.93 | 523.39 | 19029.43 | 1.44 |
| 39 | 0.00 | 298.15 | 101.30 | 99.77 | 0.35 | 0.00 | 0.00 | 0.00 |
| 40 | 0.00 | 336.55 | 101.30 | 253.70 | 0.84 | 0.00 | 3.81 | 36.53 |
| 41 | 0.00 | 353.15 | 101.30 | 320.51 | 1.03 | 0.01 | 750.71 | 3621.83 |
| 42 | 0.00 | 353.15 | 101.30 | 50.68 | 6.56 | 0.05 | 52.50 | 41.87 |
| 43 | 0.00 | 353.15 | 101.30 | 791.42 | 67.20 | 5.88 | 6202.00 | 41.87 |
| 44 | 359.36 | 298.15 | 101.30 | 104.84 | 0.37 | 17952.54 | 0.00 | 0.00 |
| 45 | 359.36 | 301.15 | 101.30 | 117.39 | 0.41 | 17975.07 | 83327.65 | 0.18 |
| 46 | 41.71 | 281.15 | 101.30 | 33.71 | 0.12 | 2171.60 | 0.00 | 0.00 |
| 47 | 41.71 | 276.15 | 101.30 | 12.71 | 0.05 | 2232.90 | 25527.17 | 0.45 |
| 48 | 58.48 | 298.15 | 101.30 | 104.84 | 0.37 | 2921.25 | 0.00 | 0.00 |
| 49 | 58.48 | 308.15 | 101.30 | 146.67 | 0.51 | 2961.38 | 23260.81 | 0.31 |
| 50 | 2.53 | 305.00 | 101.30 | 133.50 | 0.46 | 127.25 | 0.00 | 0.00 |
| 51 | 2.53 | 308.00 | 101.30 | 146.05 | 0.50 | 128.11 | 12123.18 | 3.76 |
| 52 | 0.29 | 288.00 | 101.30 | 62.39 | 0.22 | 14.52 | 0.00 | 0.00 |
| 53 | 0.29 | 283.00 | 101.30 | 41.46 | 0.15 | 14.79 | 704.99 | 1.89 |
| 54 | 8.43 | 303.15 | 4.25 | 283.71 | 0.96 | 443.50 | 19403.59 | 1.74 |
| 55 | 10.00 | 303.15 | 4.25 | 258.82 | 0.88 | 522.30 | 27161.93 | 2.06 |

electricity and cooling have been evaluated and presented in this subsection.

Fig. 8 demonstrates the effect of varying the mass flow rate of the inlet geothermal water between 5 $kg/s$ and 15 $kg/\ s$ on the cooling, freshwater, and hydrogen production rates, exergy efficiency, SUCP, and PP. Referring to Fig. 8, the increase in studied mass flow rate augments the production rate of the products and decreases the exergy efficiency, SUCP, and PP. Indeed, this increase leads to an enhancement in the enthalpy rate of the states in Fig. 1; therefore, the output streams of separator 1 experience higher enthalpy rates at higher mass flow rates. Therefore, both power production and heat recovery scenarios improve, achieving higher input energy rates by subsystems in higher mass flow rates and producing more products. However, due to overcoming the input exergy rate than the exergy rate of the products with increasing the studied mass flow rate, the exergy efficiency faces a slight reduction. Moreover, the cost rate of the total products descends; as a result, the SUCP goes up. However, the reduction in PP evident in Fig. 8 is attributed to reaching higher annual incomes in higher mass flow rates compared to the fixed cost of the system. Nevertheless, increasing the mass flow rate of the inlet geothermal water between 5 $kg/s$ and 15 $kg/s$, the cooling load, freshwater generation rate, and hydrogen production rate vary between $440-1210\ kW$, $0.13-0.43\ kg/s$, and $0.075-0.275\ kg/h$, respectively.

**Table 7**
Exergy and exergoeconomic analyses' results for each component of the multi-generation system.

| Component | $c_{F,k}$($/GJ) | $c_{P,k}$($/GJ) | $\dot{C}_D$($/year) | $\dot{Ex}_{D,k}$(KW) | $\dot{Z}_k$($/year) | $\varepsilon_k$(%) |
|---|---|---|---|---|---|---|
| Cond 1 | 98.46 | 3697.00 | 5104.00 | 51.84 | 76004.00 | 30.30 |
| Cond 2 | 91.43 | 579.70 | 8776.00 | 95.98 | 10817.00 | 29.48 |
| Cond 3 | 956.60 | 14017.00 | 479.00 | 0.50 | 544.70 | 63.33 |
| Dhu | 1501.00 | 2812.00 | 47920.00 | 31.93 | 4608.00 | 55.65 |
| Eje 1 | 27.94 | 98.46 | 12102.00 | 433.10 | 1.39 | 28.38 |
| Eje 2 | 955.80 | 956.60 | 3290.00 | 3.44 | 0.03 | 99.90 |
| Eva 1 | 115.60 | 416.40 | 2176.00 | 18.83 | 16267.00 | 76.50 |
| Eva 2 | 956.70 | 2653.00 | 117.40 | 0.12 | 333.40 | 68.40 |
| Heater | 384.50 | 91270.00 | 10.07 | 0.03 | 737.50 | 23.89 |
| Hum | 672.00 | 1501.00 | 9175.00 | 13.65 | 50486.00 | 84.06 |
| Hx 1 | 36.36 | 63.37 | 5337.00 | 146.80 | 8608.00 | 77.86 |
| Hx 2 | 91.32 | 160.40 | 169.10 | 1.85 | 172.60 | 72.75 |
| Hx 3 | 36.36 | 176.40 | 289.20 | 7.96 | 8630.00 | 88.90 |
| Hx 4 | 36.36 | 920.40 | 0.17 | 0.00 | 3.49 | 47.31 |
| KT | 91.32 | 421.10 | 3954.00 | 43.30 | 94506.00 | 87.33 |
| Mix | 91.43 | 91.43 | 0.00 | 0.00 | 0.00 | 100.00 |
| PEM | 384.70 | 1054.00 | 1642.00 | 4.27 | 2331.00 | 58.14 |
| Pu 1 | 311.40 | 1533.00 | 2405.00 | 7.73 | 6801.00 | 49.38 |
| Pu 2 | 311.40 | 2530.00 | 81.78 | 0.26 | 693.20 | 57.08 |
| Sep 1 | 36.36 | 36.36 | 0.00 | 0.00 | 0.00 | 100.00 |
| Sep 2 | 89.95 | 91.32 | 3303.00 | 36.72 | 0.00 | 98.50 |
| ST | 36.36 | 311.40 | 2714.00 | 74.64 | 137380.00 | 87.22 |
| Val 1 | 34.52 | 36.36 | 4161.00 | 120.50 | 444.10 | 95.42 |
| Val 2 | 98.46 | 115.60 | 254.80 | 2.59 | 16.37 | 85.97 |
| Val 3 | 91.32 | 92.88 | 214.00 | 2.34 | 11.93 | 98.40 |
| Val 4 | 956.60 | 956.70 | 93.15 | 0.10 | 0.97 | 100.00 |
| Val 5 | 36.36 | 43.75 | 2905.00 | 79.89 | 374.20 | 84.74 |

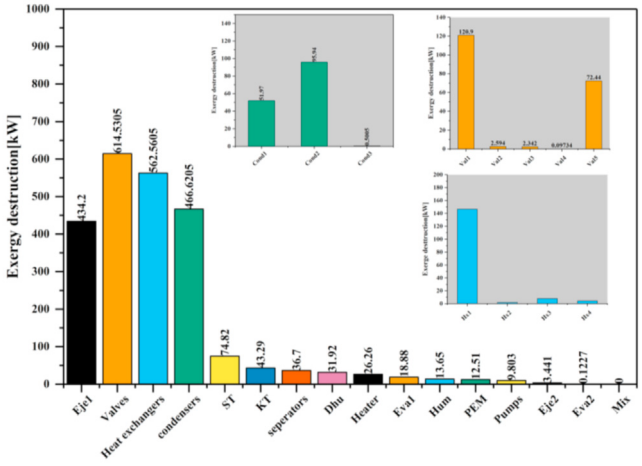


**Fig. 5.** Exergy destruction rate of the components established in the geothermal-based multi-generation system in this study.

Also, the exergy efficiency slightly declines around 40.35%, SUCP decreases from 5.62 $/*GJ* to 4.26 $/*GJ*, and the PP reduces from 2.28 *years* to 1.66 *years*.

In Fig. 9, the variation in the production rate of the cooling, freshwater, and hydrogen, exergy efficiency, SUCP, and PP is shown based on increasing the outlet pressure of the production well ranging between 1000 kPa and 1500 kPa. According to Fig. 9, growing this pressure affects the quality of the geothermal water flowing into separator 1, whereby the mass flow rate of the liquid and steam phases leaving this separator changes. Hence, the mass flow rate of the steam phase increases; consequently, the first ERC generates more cooling. Also, the HDH unit receives a lower thermal energy rate and reduces its production capacity. Furthermore, the PEME produces extra hydrogen at higher pressures owing to receiving more electricity for electrolyzing. Because of the increase in input exergy rate and its dominant effect compared to the exergy rate of the products, the exergy efficiency declines. Also, a reduction in the cost rate of the products reduces the SUCP. Although the cost rate of the products reduces, the electricity's selling price escalates the annual income and decreases the PP. Hence, the cooling and hydrogen production rates rise from 795 *kW* and 0.161 *kg*/*h* at 1000 *kPa* to 990 *kW* and 0.202 *kg*/*h* at 1500 *kPa*, respectively. Furthermore, the freshwater production rate decreases from 0.291 *kg*/*s* to 0.279 *kg*/*s*, exergy efficiency from 40.6% to 40.0%, SUCP from 5.05 $/*GJ* to 4.50 $/*GJ*, and PP from 1.97 *years* to 1.75 *years*.

The change in the production rate of the cooling, freshwater, and hydrogen, exergy efficiency, SUCP, and PP versus the inlet pressure of separator 2 is revealed in Fig. 10. The enhancement in this pressure augments the steam phase and declines the liquid phase leaving separator 1; as a result, the top of the cycle, i.e., steam turbine and first ERC, receives more enthalpy rate and generates more power and cooling. Hence, the bottom side of the cycle receives a low heat-based energy rate, producing lower products at the bottom subsystems. The increase in products of the flash-binary geothermal cycle and ERC with growing the evaluated pressure significantly increases the quality of total products and augments the exergy efficiency. However, the waste heat of the system goes up at higher pressures and slightly decreases the exergy efficiency. On the other hand, because of the significant impact of the exergy rate on the SUCP based on increasing this pressure, SUCP witnesses a reduction. Also, higher annual incomes at higher pressures reduce the PP of the system. Besides, the cooling load increases from 831 *kW* to 890 *kW*, and SUCP decreases from 4.91 $/*GJ* to 4.75 $/*GJ* at the mentioned range for separator 1 inlet pressure. Generally, the variation in other variables is insignificant.

Fig. 11 represents the influence of the pressure ratio of the steam

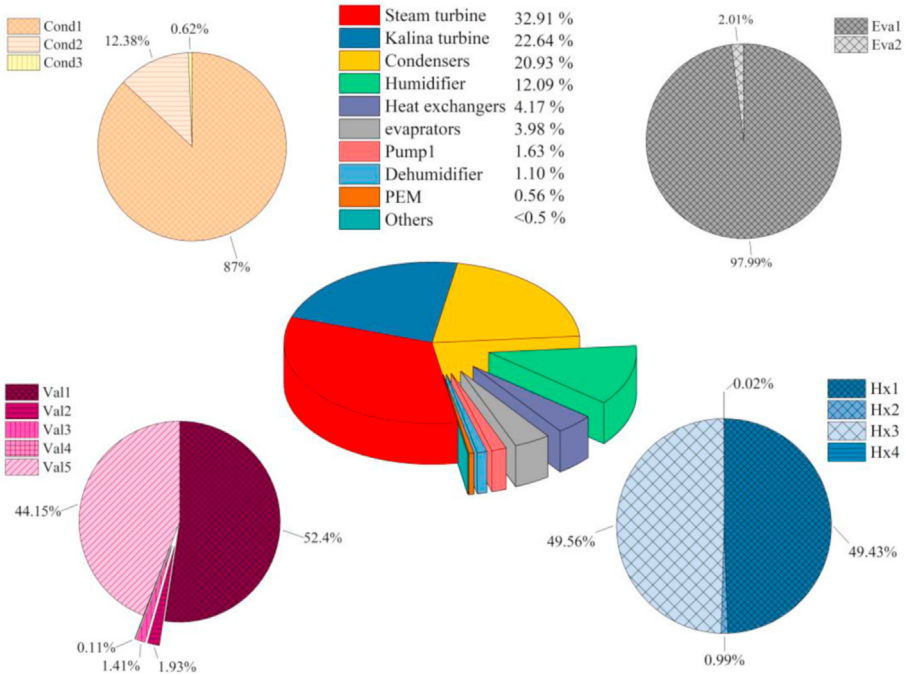


**Fig. 6.** Distribution of the purchase cost rate of the components established in the geothermal-based multi-generation system in this study.

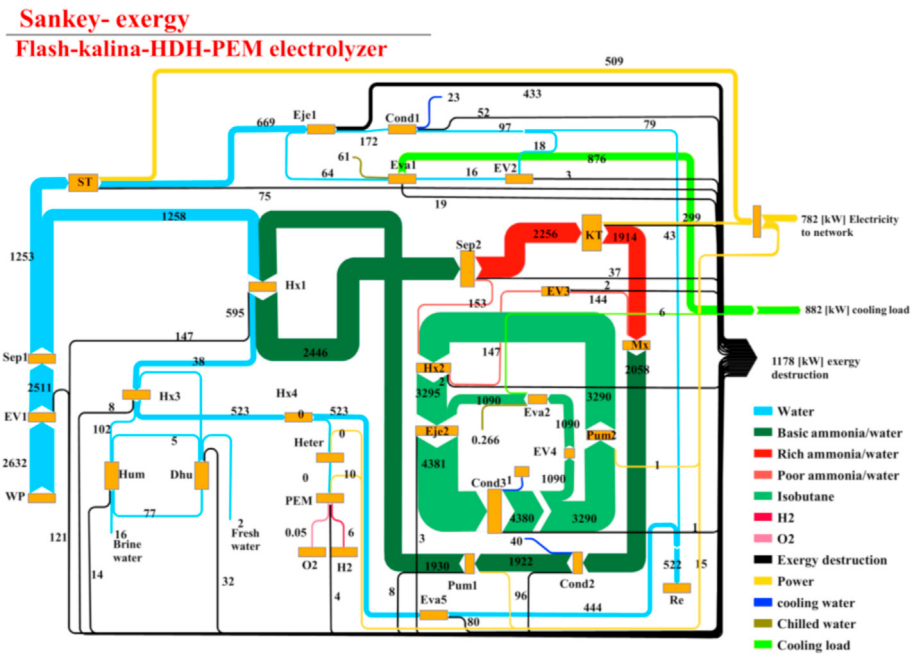


**Fig. 7.** Exergy flow through Sankey diagram of the geothermal-based multi-generation system in this study.

turbine (between 8 – 12) on the performance metrics of the polygeneration system in this paper. When this pressure ratio increases, the enthalpy difference of the steam turbine goes up, and more power can be generated. Hence, the waste heat of the steam turbine reduces; consequently, low heat can transfer to the first ERC to produce cooling. Since this variation has no effect on the amount of the liquid phase leaving separator 1, the heat recovery by bottom subsystems remains constant. Hence, the electricity and cooling generated by the Kalina cycle and the second ERC and freshwater generated by the HDH unit remain constant. However, due to achieving higher electricity at higher pressures by the PEME, its water electrolysis increases, producing higher hydrogen. Higher exergy efficiencies at higher pressure ratios are owing to the lower exergy destruction rate in this situation. Also, the increase in this pressure ratio increases the cost rate of the products, increasing the SUCP. On the other hand, the yearly investment cost rate of the

**Table 8**
The results of the performance indicators for the multi-generation system.

| Performance items | Value | Unit |
|---|---|---|
| Net output power, $\dot{W}_{net}$ | 782.0 | kW |
| Cooling load, $\dot{Q}_{cooling}$ | 881.6 | kW |
| Rate of produced fresh water, $\dot{m}_{fw}$ | 0.286 | kg/s |
| Rate of produced Hydrogen, $\dot{m}_{H2}$ | 0.181 | kg/h |
| Energy efficiency, $\eta_{th}$ | 31.74 | % |
| Exergy efficiency, $\eta_{ex}$ | 40.36 | % |
| PP | 1.86 | year |
| SUCP | 4.76 | $/GJ |

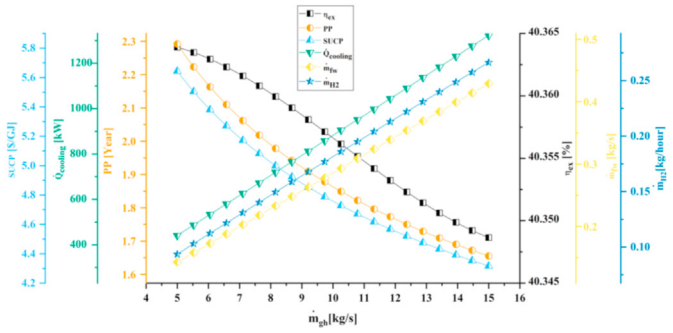

**Fig. 8.** Variation in the performance metrics with the mass flow rate of the geothermal water.

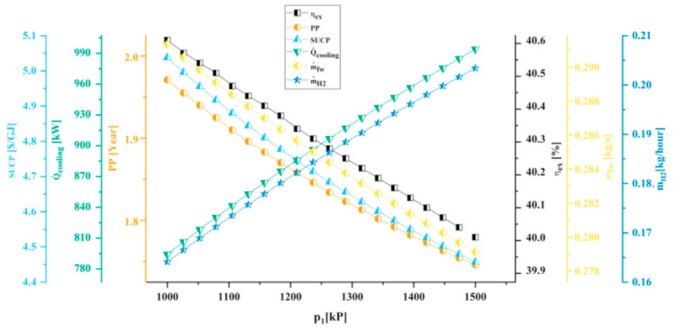

**Fig. 9.** Variation in performance metrics of the system with the pressure of the production well.

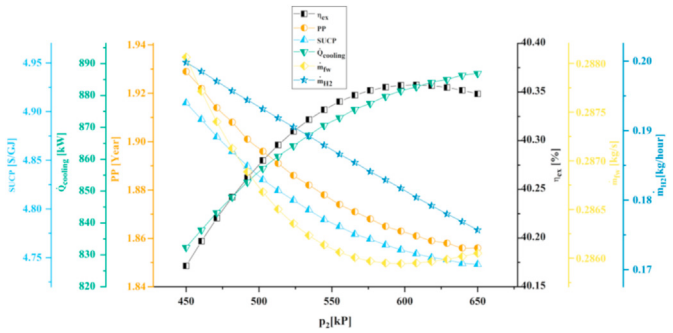

**Fig. 10.** Variation in performance metrics of the system with the pressure of separator 1.

system rises; therefore, the PP of the system escalates. Accordingly, the cooling load prepared by the system declines from 990 *kW* at the pressure ratio of 8 to 780 *kW* at the pressure ratio of 12. Also, this variation raises the hydrogen production rate from 0.166 *kg/ h* to 0.198 *kg/h* at the mentioned range for the pressure ratio evaluated here. In this case, the exergy efficiency, SUCP, and PP correspondingly enhance from 38.51%, 4.31 $/*GJ*, and 1.72 *years*, to 41.75%, 5.18 $/*GJ*, and 1.99 *years*.

Fig. 12 depicts the change in performance metrics of the system when the temperature of evaporator 1 increases from 273 *K* to 278 *K*. This variation only varies the operating condition of the first ERC; therefore, other subsystems don't experience any change in their capacity. Hence, the cooling load rises from 875 *kW* to 1170 *kW*. Due to the insignificant impact of the generated cooling on the overall performance of the whole system, other variables witness a negligible trend. In this regard, the SUCP decreases from 4.67 $/*GJ* to 3.92 $/*GJ* and the PP from 1.85 *years* to 1.55 *years*.

Based on the change in performance metrics of the system proposed in this paper with the enhancement in the terminal temperature difference of heat exchanger 1 ranging between 10 *K* and 20 *K*, Fig. 13 is plotted and presented. Referring to this figure, the heat recovered by the Kalina cycle and the second ERC goes down, decreasing the cooling production of this unit from 885.0 *kW* to 881.5 *kW*. Accordingly, heat exchanger 3 as the heater of the HDH unit receives lower heat at higher terminal temperature differences, and the freshwater production rate descends. Since the PEME receives constant electricity at each temperature studied here, its production capacity doesn't change. As Fig. 13 displays, the change in variables related to the system's performance is negligible, respecting the increase in the terminal temperature difference of heat exchanger 1.

Fig. 14 reveals the results of the NPV analysis for the system lifetime and PP based on the electricity and cooling selling prices. Negative NPVs show the period of the lifetime at which the system cannot reach the revenue; after that, the system's profitability period is started. Simply put, the NPV equal to zero stands for the

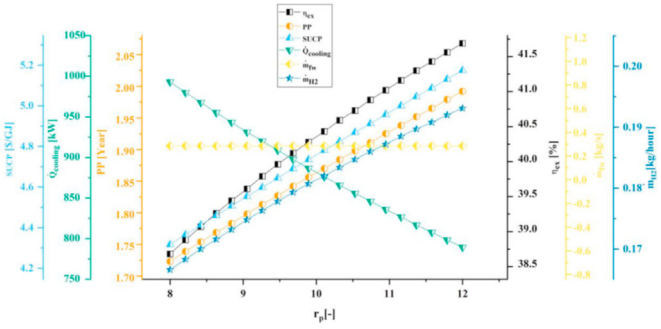

**Fig. 11.** Variation in performance metrics of the system with the pressure ratio of the steam turbine.

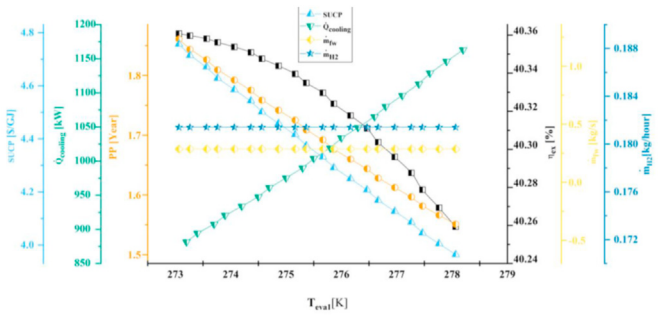

**Fig. 12.** Variation in performance metrics of the system with the evaporator 1 inlet temperature.

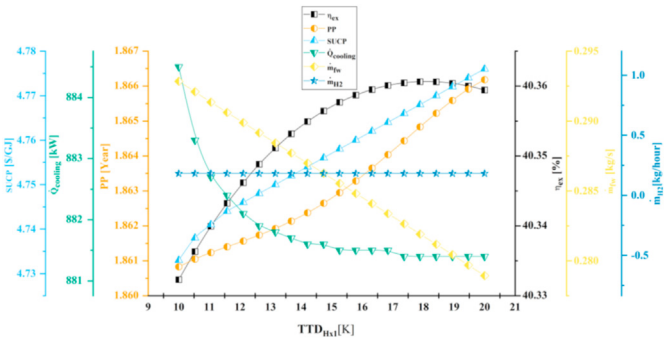


**Fig. 13.** Variation in performance metrics of the system with the terminal temperature difference of heat exchanger 1.

year corresponding to the PP of the system. Referring to Fig. 14a, four different selling prices have been considered for the electricity, in which the selling price of 0.15 $/kWh remarkably increases the NPV. Also, reducing the selling price from 0.15 $/kWh to 0.07 $/kWh declines the PP from 1.86 years to 1.28 years. According to Fig. 14b, four different selling prices of cooling load (0.11 $/kWh, 0.15 $/kWh, 0.18 $/kWh, and 0.20 $/kWh) have been considered, wherein the best and worst PP belong to selling prices of 0.20 $/kWh and 0.11 $/kWh with the values of 1.20 years and 1.86 years, respectively. Lastly, Fig. 14c shows the curves of the PP of the system versus increasing the selling price of electricity ranging between 0.05 $/kWh and 0.15 $/kWh and cooling between 0.09 $/kWh to 0.20 $/kWh. Respecting the variation in the selling price of the electricity, PP reduces from 2.10 years to 1.30 years. Also, based on the selling price of the cooling, the PP drops from 2.15 years to 1.20 years.

### 5.3. Optimization results

Genetic algorithm together with LINMAP and TOPSIS decision-makers is considered for optimizing the polygeneration system. Four optimization cases are evaluated, whereby Fig. 15 shows the Pareto front diagrams of them. These cases include exergy/cost (shown in Fig. 15a), exergy/cooling (shown in Fig. 15b), exergy/freshwater (shown in Fig. 15c), and exergy/hydrogen (shown in Fig. 15d). Ideal and non-ideal solutions are demonstrated, and final optimal solutions for each case are determined using LINMAP and TOPSIS.

Based on Fig. 15a, the optimum exergy efficiency is found to be 46.44% and 45.89% based on LINMAP and TOPSIS methods, respectively, which are higher than the base case exergy efficiency (40.36%). Also, in this scenario, the SUCP is selected to be 3.98 $/GJ$ and 3.74 $/GJ$ based on LINMAP and TOPSIS methods, respectively that are far lower than for base case SUCP (4.76 $/GJ$).

In the second case (Fig. 15b), the selected optimum exergy efficiency and cooling load by LINMAP are equal to 48.14% and 974.88$kW$, respectively. Also, in this scenario, the TOPSIS method selects 47.48% and 1011.08$kW$ as the optimum points for the exergy efficiency and cooling load.

Referring to exergy and freshwater optimization scenario in Fig. 15c, the optimum exergy efficiency and freshwater production rate are selected as 47.22% and 0.361$kg/s$, respectively based on LINMAP method. However, the TOPSIS method selects $\eta_{ex} = 48.24$ and $\dot{m}_{fw} = 0.35 kg/s$ as the optimum point.

As the last optimization scenario, Fig. 15d depicts the optimum exergy efficiency and hydrogen generation rate of 49.71% and

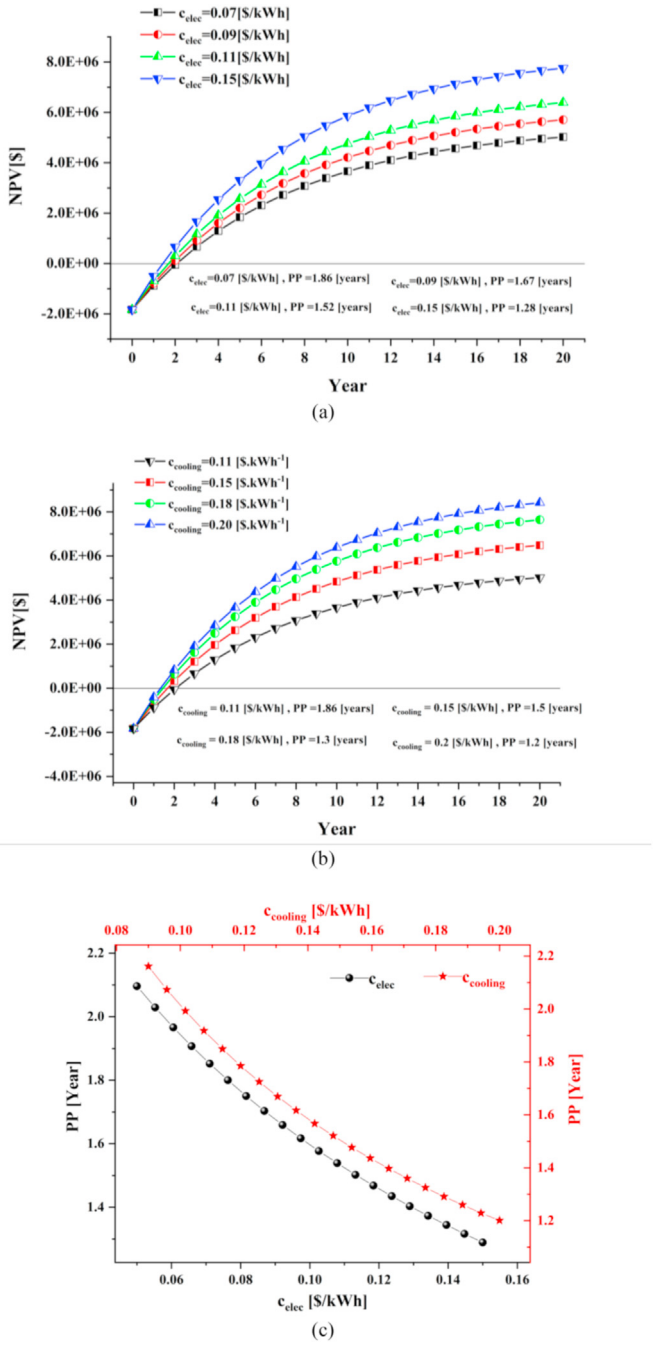


**Fig. 14.** (a) NPV results for different electricity selling price, (b) NPV results for different selling price, and (c) variation in PP with the selling price of electricity and cooling.

0.186$kg/h$, respectively based on LINMAP method. While, the optimum exergy efficiency and hydrogen generation rate are obtained to be 48.53% and 0.203$kg/h$, respectively based on TOPSIS method.

Scatter plots are shown in Fig. 16 to indicate the distribution of local optimum points over the population size, which concludes the optimization section. To design the system for optimum performance, the appropriate operating range for each parameter should be considered. Some of these parameters are very sensitive to value changes and may cause the system to be inefficient.

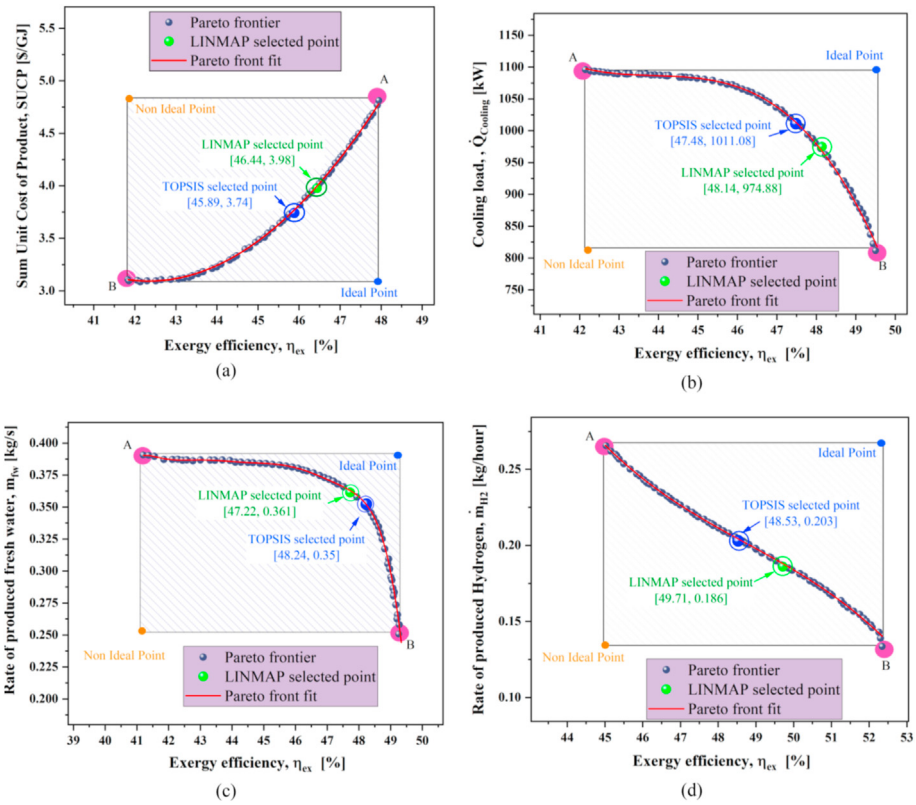


**Fig. 15.** Pareto front diagrams achieved for the (a) exergy/cost case, (b) exergy/freshwater case, and (c) exergy/hydrogen case. (d) exergy/cooling case.

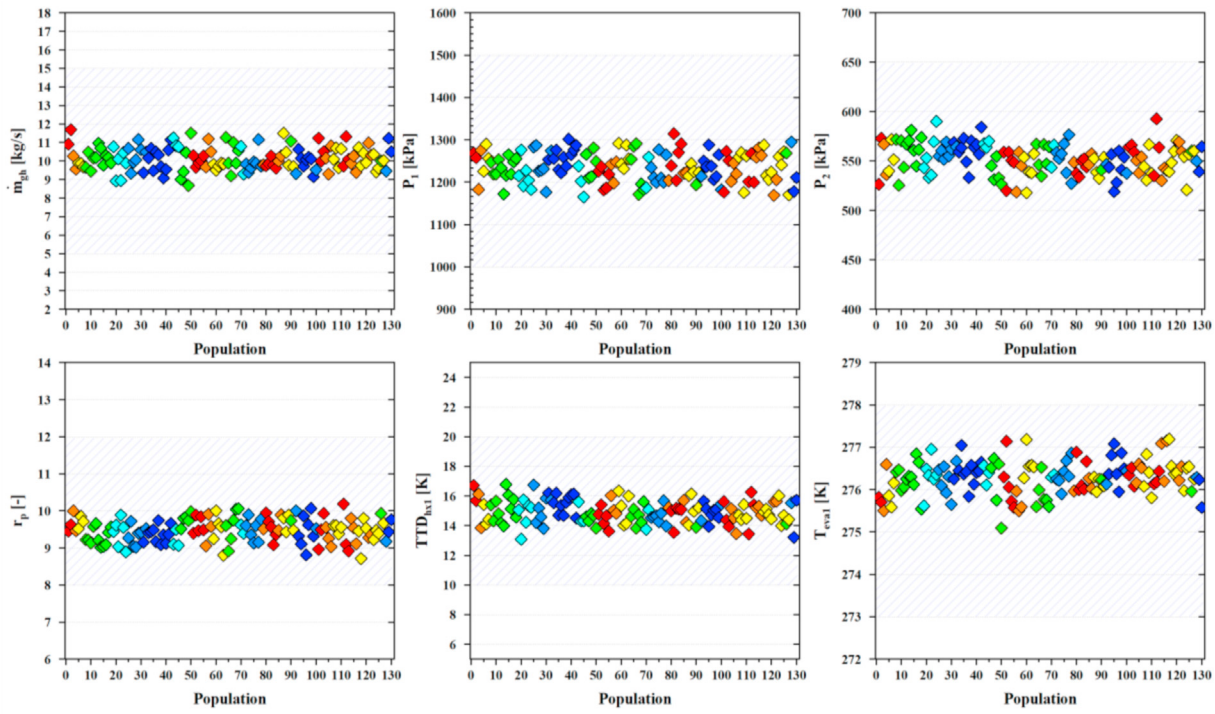


**Fig. 16.** Scatter distribution for the decicion variabes based on the GA method.

## 6. Conclusions

The current work deals with a novel geothermal-based polygeneration system through five stages of innovative heat recovery. In essence, the whole system consisted of a flash-binary geothermal cycle, an ejector refrigeration cycle (ERC), a Kalina cycle integrated with another ERC, a humidification dehumidification (HDH) desalination unit, and a proton exchange membrane electrolyzer (PEME). The capability characterization of the system was accomplished through sensitivity analysis and multi-objective optimization, wherein energy, exergy, exergoeconomic, and net present value (NPV) analyses among with a genetic algorithm were applied. The sensitivity analysis was carried out based on a parametric study at which six parameters are selected including mass flow rate of the inlet geothermal water, its pressure, separator 1 inlet pressure, pressure ratio of the steam turbine, evaporator 1 inlet temperature, and terminal temperature difference of heat exchanger 1. Likewise, the studied variables to predict the feasibility of the system were the production rate of the cooling, freshwater, and hydrogen, exergy efficiency, sum unit cost of products (SUCP), and payback period (PP) of the system. After validating the simulation in engineering equation solver (EES) software and optimization by MATLAB software, and discussing the results attained, the following points are the main outcomes of this paper.

- The system designed in this study was more sensitive to varying the mass flow rate of the inlet geothermal water. Also, the pressure of the geothermal water extracted and pressure ratio of the steam turbine had a remarkable effect on the performance indicators of the system. However, the variation in these variables with increasing separator 1 inlet pressure, evaporator 1 inlet temperature, and terminal temperature difference of heat exchanger 1 was insignificant.
- When the mass flow rate of the inlet geothermal water increases, the produced cooling load, hydrogen, and freshwater experienced an enhancement, and exergy efficiency, SUCP, and PP of the system declined.
- The increase in the pressure of geothermal water extracted augmented the cooling and freshwater production rate and reduced the freshwater generation rate, exergy efficiency, SUCP, and PP of the system.
- Enhancing the pressure ratio of the steam turbine decreased the cooling load and increased the hydrogen generation rate, exergy efficiency, SUCP, and PP of the system. Also, this parameter did not affect the production rate of freshwater.
- Ejector 1 was the major irreversibility source of the whole system devised and steam turbine had the highest investment cost rate among components.
- Among the optimization cases, the highest exergy efficiency belonged to the exergy/hydrogen case with a value of 49.71%. However, the exergy/cost case as the most important optimization case calculated the optimum exergy efficiency and SUCP of 46.44% and 3.98 $/GJ, respectively based on LINMAP method.

## Author statement

Kun Li conceived the research idea, conducted the initial analysis, collected data, and authored the majority of the text. Yi-Zhe Ding authored parts of the text, reviewed the analysis, proposed changes, and contributed to data collection. Chen Ai developed the parametric analysis models and the code for the figures and checked and contributed to the analysis. Hongwei Sun reviewed and edited the manuscript and contributed parts of the text. Yi-Peng Xu reviewed and edited the manuscript and proposed changes for its organization and structure. Navid Nedaei conceptualized the study, co-developed the methodology for the screening of the data set, proposed the conceptual design of the model, and provided significant input into the research coordination.

## Declaration of competing interest

The authors declare that they have no known competing financial interests or personal relationships that could have appeared to influence the work reported in this paper.

## Acknowledgement

This work is supported Weifang University of Science and Technology Doctoral research start-up funds project under Grant2021KJBS12, and Weifang University of Science and Technology Discipline Construction Blockchain Special Project under Grant 2021XKJS10.

## Appendix A. Supplementary data

Supplementary data to this article can be found online at https://doi.org/10.1016/j.energy.2022.123198.

## References

[1] Hajabdollahi H, Ganjehkaviri A, Jaafar MNM. Thermo-economic optimization of RSORC (regenerative solar organic Rankine cycle) considering hourly analysis. Energy 2015;87:369–80.
[2] Khorasaninejad E, Hajabdollahi H. Thermo-economic and environmental optimization of solar assisted heat pump by using multi-objective particle swam algorithm. Energy 2014;72:680–90.
[3] Khaligh A, Onar OC. Energy harvesting: solar, wind, and ocean energy conversion systems. CRC press; 2017.
[4] Luqman M, Ghiat I, Maroof M, Lahlou F, Bicer Y, Al-Ansari T. Application of the concept of a renewable energy based-polygeneration system for sustainable thermal desalination process-A thermodynamics' perspective. Int J Energy Res 2020;44:12344–62.
[5] Bull SR. Renewable energy today and tomorrow. Proc IEEE 2001;89:1216–26.
[6] Barbier E. Geothermal energy technology and current status: an overview. Renew Sustain Energy Rev 2002;6:3–65.
[7] Tester JW, Anderson BJ, Batchelor AS, Blackwell DD, DiPippo R, Drake EM, et al. The future of geothermal energy, vol. 358. Massachusetts Inst Technol; 2006.
[8] Glassley WE. Geothermal energy: renewable energy and the environment. CRC press; 2014.
[9] Stober I, Bucher K. Geothermal energy, vol. 10. Ger Springer-Verlag Berlin Heidelberg; 2013. p. 973–8.
[10] Wang J, Wang J, Dai Y, Zhao P. Thermodynamic analysis and optimization of a flash-binary geothermal power generation system. Geothermics 2015;55:69–77.
[11] Yuksel YE, Ozturk M. Thermodynamic and thermoeconomic analyses of a geothermal energy based integrated system for hydrogen production. Int J Hydrogen Energy 2017;42:2530–46.
[12] Boyaghchi FA, Safari H. Parametric study and multi-criteria optimization of total exergetic and cost rates improvement potentials of a new geothermal based quadruple energy system. Energy Convers Manag 2017;137:130–41.
[13] Aali A, Pourmahmoud N, Zare V. Exergoeconomic analysis and multi-objective optimization of a novel combined flash-binary cycle for Sabalan geothermal power plant in Iran. Energy Convers Manag 2017;143:377–90.
[14] Van Erdeweghe S, Van Bael J, Laenen B, D'haeseleer W. Optimal combined heat-and-power plant for a low-temperature geothermal source. Energy 2018;150:396–409.
[15] Salehi S, Mahmoudi SMS, Yari M, Rosen MA. Multi-objective optimization of two double-flash geothermal power plants integrated with absorption heat transformation and water desalination. J Clean Prod 2018;195:796–809.
[16] Calise F, Di Fraia S, Macaluso A, Massarotti N, Vanoli L. A geothermal energy system for wastewater sludge drying and electricity production in a small island. Energy 2018;163:130–43.
[17] Leveni M, Manfrida G, Cozzolino R, Mendecka B. Energy and exergy analysis of cold and power production from the geothermal reservoir of Torre Alfina. Energy 2019;180:807–18.
[18] Ebadollahi M, Rostamzadeh H, Pedram MZ, Ghaebi H, Amidpour M. Proposal and assessment of a new geothermal-based multigeneration system for cooling, heating, power, and hydrogen production, using LNG cold energy recovery. Renew Energy 2019;135:66–87.

[19] Temiz M, Dincer I. Techno-economic assessment of bifacial photovoltaic and geothermal based multigeneration system for cleaner communities. J Clean Prod 2020;275:122879.
[20] Kurşun B. Energy and exergy analysis of a concentrated photovoltaic recuperator design for a geothermal based multi-generation system. Appl Therm Eng 2020;181:115932.
[21] Wang J, Ren C, Gao Y, Chen H, Dong J. Performance investigation of a new geothermal combined cooling, heating and power system. Energy Convers Manag 2020;208:112591.
[22] Karapekmez A, Dincer I. Thermodynamic analysis of a novel solar and geothermal based combined energy system for hydrogen production. Int J Hydrogen Energy 2020;45:5608–28.
[23] Li Z, Khanmohammadi S, Khanmohammadi S, Al-Rashed AAAA, Ahmadi P, Afrand M. 3-E analysis and optimization of an organic rankine flash cycle integrated with a PEM fuel cell and geothermal energy. Int J Hydrogen Energy 2020;45:2168–85.
[24] Cao Y, Haghghi MA, Shamsaiee M, Athari H, Ghaemi M, Rosen MA. Evaluation and optimization of a novel geothermal-driven hydrogen production system using an electrolyser fed by a two-stage organic Rankine cycle with different working fluids. J Energy Storage 2020;32:101766.
[25] Parikhani T, Delpisheh M, Haghghi MA, Holagh SG, Athari H. Performance enhancement and multi-objective optimization of a double-flash binary geothermal power plant. Energy Nexus 2021;2:100012.
[26] Cao Y, Xu D, Togun H, Dhahad HA, Azariyan H, Farouk N. Feasibility analysis and capability characterization of a novel hybrid flash-binary geothermal power plant and trigeneration system through a case study. Int J Hydrogen Energy 2021.
[27] Azariyan H, Vajdi M, Takleh HR. Assessment of a high-performance geothermal-based multigeneration system for production of power, cooling, and hydrogen: thermodynamic and exergoeconomic evaluation. Energy Convers Manag 2021;236:113970.
[28] Musharavati F, Khanmohammadi S, Pakseresht A. A novel multi-generation energy system based on geothermal energy source: thermo-economic evaluation and optimization. Energy Convers Manag 2021;230:113829.
[29] Leveni M, Cozzolino R. Energy, exergy, and cost comparison of Goswami cycle and cascade organic Rankine cycle/absorption chiller system for geothermal application. Energy Convers Manag 2021;227:113598.
[30] Cao Y, Dhahad HA, Togun H, Hussen HM, Anqi AE, Farouk N, et al. Thermodynamic and economic assessments and multi-criteria optimization of a novel poly-generation plant using geothermal energy and multi heat recovery technique. Int J Hydrogen Energy 2021;46:27851–73.
[31] Ansarinasab H, Hajabdollahi H, Fatimah M. Life cycle assessment (LCA) of a novel geothermal-based multigeneration system using LNG cold energy-integration of Kalina cycle, stirling engine, desalination unit and magnetic refrigeration system. Energy 2021;231:120888.
[32] Ansarinasab H, Hajabdollahi H. Multi-objective optimization of a geothermal-based multigeneration system for heating, power and purified water production purpose using evolutionary algorithm. Energy Convers Manag 2020;223:113476.
[33] Rostamzadeh H, Ebadollahi M, Ghaebi H, Shokri A. Comparative study of two novel micro-CCHP systems based on organic Rankine cycle and Kalina cycle. Energy Convers Manag 2019. https://doi.org/10.1016/j.enconman.2019.01.003.
[34] Hamrang F, Shokri A, Mahmoudi SM, Ehghaghi B, Rosen MA. Performance analysis of a new electricity and freshwater production system based on an integrated gasification combined cycle and multi-effect desalination. Sustainability 2020;12:7996.
[35] Ahmadi S, Ghaebi H, Shokri A. A comprehensive thermodynamic analysis of a novel CHP system based on SOFC and APC cycles. Energy 2019;186:115899. https://doi.org/10.1016/j.energy.2019.115899.
[36] Narayan GP, Sharqawy MH, Lienhard VJH, Zubair SM. Thermodynamic analysis of humidification dehumidification desalination cycles. Desalination Water Treat 2010;16:339–53.
[37] Du Y, Chen K, Dai Y. A study of the optimal control approach for a Kalina cycle system using a radial-inflow turbine with variable nozzles at off-design conditions. Appl Therm Eng 2019;149:1008–22.
[38] Yilmaz C, Kanoglu M, Abusoglu A. Exergetic cost evaluation of hydrogen production powered by combined flash-binary geothermal power plant. Int J Hydrogen Energy 2015;40:14021–30.
[39] Kianfard H, Khalilarya S, Jafarmadar S. Exergy and exergoeconomic evaluation of hydrogen and distilled water production via combination of PEM electrolyzer, RO desalination unit and geothermal driven dual fluid ORC. Energy Convers Manag 2018;177:339–49.
[40] Moran MJ, Shapiro HN, Boettner DD, Bailey MB. Fundamentals of engineering thermodynamics. John Wiley & Sons; 2010.
[41] Bejan A, Tsatsaronis G, Moran MJ. Thermal design and optimization. John Wiley & Sons; 1995.
[42] Cengel YA, Ghajar AJ. Heat and mass transfer. A Pract Approach; 2007.
[43] van Kleef LMT, Oyewunmi OA, Markides CN. Multi-objective thermo-economic optimization of organic Rankine cycle (ORC) power systems in waste-heat recovery applications using computer-aided molecular design techniques. Appl Energy 2019;251:112513.
[44] Wang A, Wang S, Ebrahimi-Moghadam A, Farzaneh-Gord M, Moghadam AJ. Techno-economic and techno-environmental assessment and multi-objective optimization of a new CCHP system based on waste heat recovery from regenerative Brayton cycle. Energy 2021:122521.
[45] Habibollahzade A, Mehrabadi ZK, Markides CN. Comparative thermoeconomic analyses and multi-objective particle swarm optimization of geothermal combined cooling and power systems. Energy Convers Manag 2021;234:113921.
[46] Wu Z, Zhu P, Yao J, Zhang S, Ren J, Yang F, et al. Combined biomass gasification, SOFC, IC engine, and waste heat recovery system for power and heat generation: energy, exergy, exergoeconomic, environmental (4E) evaluations. Appl Energy 2020;279:115794.
[47] Shi K, Asgari A. Energy, exergy, and exergoeconomic analyses and optimization of a novel thermal and compressed air energy storage integrated with a dual-pressure organic Rankine cycle and ejector refrigeration cycle. J Energy Storage 2021:103610.
[48] Fan G, Yang B, Guo P, Lin S, Farkoush SG, Afshar N. Comprehensive analysis and multi-objective optimization of a power and hydrogen production system based on a combination of flash-binary geothermal and PEM electrolyzer. Int J Hydrogen Energy 2021;46:33718–37.
[49] Rostamzadeh H, Namin AS, Ghaebi H, Amidpour M. Performance assessment and optimization of a humidification dehumidification (HDH) system driven by absorption-compression heat pump cycle. Desalination 2018;447:84–101.
[50] Cao Y, Dhahad HA, Togun H, Haghghi MA, Athari H, Mohamed AM. Exergetic and economic assessments and multi-objective optimization of a modified solar-powered CCHP system with thermal energy storage. J Build Eng 2021:102702.
[51] Mehrabadi ZK, Boyaghchi FA. Thermodynamic, economic and environmental impact studies on various distillation units integrated with gasification-based multi-generation system: comparative study and optimization. J Clean Prod 2019;241:118333.